

New ASKAP Radio Supernova Remnants and Candidates in the Large Magellanic Cloud

Luke M. Bozzetto,¹ Miroslav D. Filipović¹,^{*} H. Sano,² R. Z. E. Alsaberi,¹ L. A. Barnes¹ I. S. Bojičić,¹ R. Brose,³ L. Chomiuk,⁴ E. J. Crawford,¹ S. Dai,¹ M. Ghavam,¹ F. Haberl,⁵ T. Hill,¹ A. M. Hopkins,^{6,1} A. Ingallinera,⁷ T. Jarrett,^{8,1} P. J. Kavanagh,⁹ B. S. Koribalski,^{10,1} R. Kothes,¹¹ D. Leahy,¹² E. Lenc,¹⁰ I. Leonidaki,¹³ P. Maggi,¹⁴ C. Maitra,⁵ C. Matthew,¹ J. L. Payne,¹ C. M. Pennock,¹⁵ S. Points,¹⁶ W. Reid,^{1,17,18} S. Riggi,⁷ G. Rowell,¹⁹ M. Sasaki,²⁰ S. Safi-Harb,²¹ J. Th. van Loon,¹⁰ N. F. H. Tothill,¹ D. Urošević,^{22,23} F. Zangrandi,²⁰

Affiliations are listed at the end of the paper

Accepted XXX. Received YYY; in original form ZZZ

ABSTRACT

We present a new Australian Square Kilometre Array Pathfinder (ASKAP) sample of 14 radio Supernova Remnant (SNR) candidates in the Large Magellanic Cloud (LMC). This new sample is a significant increase to the known number of older, larger and low surface brightness LMC SNRs. We employ a multi-frequency search for each object and found possible traces of optical and occasionally X-ray emission in several of these 14 SNR candidates. One of these 14 SNR candidates (MCSNR J0522–6543) has multi-frequency properties that strongly indicate a bona fide SNR. We also investigate a sample of 20 previously suggested LMC SNR candidates and confirm the SNR nature of MCSNR J0506–6815. We detect lower surface brightness SNR candidates which were likely formed by a combination of shock waves and strong stellar winds from massive progenitors (and possibly surrounding OB stars). Some of our new SNR candidates are also found in a lower density environments in which SNe type Ia explode inside a previously excavated interstellar medium (ISM).

Key words: ISM: supernova remnants – (galaxies:) Magellanic Clouds

1 INTRODUCTION

Supernovae (SNe) are powerful explosions that mark the end for certain types of stars. The study of SNe and their remnants is essential to understanding the physical and chemical evolution of the ISM. SNe are typically categorised as arising either from a core-collapse event occurring in more massive, short-lived stars ($\geq 8 M_{\odot}$), or a thermonuclear type Ia event occurring in carbon-oxygen white dwarfs. Both types enrich the ISM with heavy elements, create a shock wave that heats the swept-up ISM, compress magnetic fields, and accelerate particles such as cosmic rays (e.g. Filipović & Tothill 2021a).

In the search for the imprints of these SNe explosions, a few key characteristics are used to classify an object as a SNR: a non-thermal radio spectral index of $\alpha < -0.4$ (defined as $S_{\nu} \propto \nu^{\alpha}$, where S_{ν} is flux density, ν is frequency and α is the spectral index),

diffuse X-ray emission and an elevated $[\text{Sn}]/\text{H}\alpha$ ratio ≥ 0.4 which is produced by the high-velocity shocks (e.g. Hurley-Walker et al. 2021; Maggi 2021; Yew et al. 2021). Not all SNRs exhibit all three of these characteristics. Typically, two of these characteristics are enough to confirm a SNR classification, while one of them marks the source as an SNR candidate (Reynolds et al. 2012; Maggi et al. 2016; Bozzetto et al. 2017; Maggi et al. 2019). Also, a variety of SNR types (such as Pulsar Wind Nebula (PWN)) produces other recognisable signatures such as the polarised radio emission and flatter radio spectral index.

The LMC, an irregular dwarf galaxy, has been the target of extensive studies into SNRs since they were first observed by Mathewson & Healey (1964). Details of the LMC SNR studies are covered in Bozzetto et al. (2017) & Yew et al. (2021). The LMC is of particular interest in the hunt for SNRs because of its low foreground absorption and relatively close proximity of 50 kpc (Pietrzyński et al. 2019). While the proximity of the LMC allows us to study our nearest Galactic neighbour in more detail than those further away,

* E-mail: m.filipovic@westernsydney.edu.au

for all intents and purposes, all objects within the LMC are assumed to be at the same approximate 50 kpc.

The LMC also hosts a mini-starburst at sub-solar metallicity. This may result in a dis-proportionally high number of very massive stars ($>100 M_{\odot}$; [Schneider et al. 2018](#)) and pair-instability SNe which ultimately produce SNRs. The mean energy of the LMC SNRs is $\sim 5 \times 10^{50}$ erg, very similar to Galactic SNRs ($\sim 4 \times 10^{50}$ erg; [Leahy 2017](#); [Leahy et al. 2020](#)).

The new generation of radio telescopes such as ASKAP and MeerKAT, with their higher sensitivity instrumentation, give us an unprecedented look into some of the older, larger, faded remnants – especially those that are embedded or obscured by nearby stronger sources ([Norris et al. 2021](#); [Koribalski et al. 2021](#); [Filipović et al. 2022](#); [Johnston et al. 2022](#)) and those expanding into cavities blown by the progenitor. Certainly, small size LMC SNRs (< 15 arcsec or 3.5 pc at the LMC distance) are presumably young (and therefore bright) and they are most likely discovered in the previous surveys ([Urošević 2022](#)).

In this paper, we make use of new radio continuum data taken by the ASKAP telescope ([Pennock et al. 2021](#); [Filipović et al. 2021](#)) to add 14 new candidates to the LMC SNR sample, creating the most complete SNR sample of any galaxy (see Fig. 1). Moving towards such a comprehensive population is essential for statistical analysis and the evolutionary understanding of the remains of exploded stars. A complete sample of SNRs provides the ability to study their global properties, in addition to carrying out detailed analyses of their subclasses (e.g., sorted by X-ray, optical and radio morphology or by progenitor Supernova (SN) type).

2 OBSERVATIONS AND DATA PROCESSING

This paper draws together various existing surveys of the LMC at multiple wavelengths to identify new candidate SNRs, with a primary focus on the sources identified in the new ASKAP observations of [Pennock et al. \(2021\)](#), see Fig. 1).

2.1 ASKAP data

These ASKAP radio data comprise a twelve-pointing mosaic taken of the LMC at a centre frequency of 888 MHz (bandwidth of 256 MHz, spatial resolution of 13.9×12.1 arcsec² and position angle -84°). Details of the observations, data reduction and analysis of these data have been presented in [Pennock et al. \(2021\)](#). The image shown in Fig. 1 is affected by various artefacts and missing short spacing data. However, its robust maximum angular scale of 49 arcmin combined with improved sensitivity ([Filipović et al. 2022](#)) ensures a reasonable environment to search for new LMC SNRs. At the time of these observations (April 2019) ASKAP didn't have polarisation capability, and therefore, the ASKAP image used here is total intensity (Stokes I).

2.2 ATCA data

We observed MCSNR J0522–6543¹ with the Australia Telescope Compact Array (ATCA) on 30th November 2019 and 23rd February

2020 (project codes C3275 and C3292; see Appendix A8). The observations were carried out in frequency switching mode (between 2100 MHz and 5500/9000 MHz) with 1-hour of integration over a 12-hour period using arrays 1.5C and EW367. The Compact Array Broadband Back-end (CABB) with its 2048 MHz bandwidth was used centred at $\nu=5500$ and 9000 MHz, totaling 117.62 minutes of integration. At the same time, we also used the $\nu=2100$ MHz band with a total of 112.2 minutes of integration. The primary (flux) calibrator was PKS B1934–638 ($S_{2100}=11.651$, $S_{5500}=5.010$ and $S_{9000}=2.704$ Jy) and secondary calibrator (phase) was PKS B0530–727 ($S_{2100}=0.680$, $S_{5500}=0.585$ and $S_{9000}=0.695$ Jy). For imaging, we used WSCLEAN ([Offringa et al. 2014](#)) and flagged out data from the 6th antenna for all observations to focus on the extended emission of this object at the expense of reducing the resolution. We achieved a resolution of 20.95×16.60 arcsec² at 2100 MHz, 15.85×12.79 arcsec² at 5500 MHz and 8.81×7.05 arcsec² at 9000 MHz (all at P.A.=0 degrees) with a corresponding rms noise of 0.1, 0.05 and 0.025 mJy beam⁻¹, respectively.

2.3 Optical, X-ray and IR data

The optical data used in this study consists of H α , [SII], [OIII] images from the Magellanic Cloud Emission Line Survey (MCELS) survey; more details can be found in [Points et al. \(2019\)](#).

To gain insight into the type of stellar environment hosting the suspected progenitors of these objects, we use data sourced from the Magellanic Clouds Photometric Survey (MCPS; [Zaritsky et al. 2004](#)). To this end, we construct colour-magnitude diagrams and identify blue stars more massive than $\sim 8 M_{\odot}$ within a 100 pc (6.9 arcmin at the distance of the LMC; $\sim 10^7$ yr at 10 km s^{-1}) radius of each of the objects presented in this study. The size of SNRs can well exceed 150 pc in diameter and therefore our chosen search area will give us a good view of the environment and possible origin of these objects as demonstrated in [Bozzetto et al. \(2017\)](#). This allows us to see the prevalence of early-type stars close to the candidate remnants.

We also consult various X-ray surveys including *ROSAT* ([Haberl & Pietsch 1999](#)) and *XMM-Newton* ([Haberl 2019](#)). Finally, we use the Spitzer infrared survey of the LMC, “Surveying the Agents of a Galaxy’s Evolution” (SAGE) ([Meixner et al. 2006](#)).

2.4 H I data

For atomic hydrogen, we used the ATCA & Parkes H I survey data from [Kim et al. \(2003\)](#) with its angular resolution of 60×60 arcsec². We made the velocity channel maps and position-velocity ($p - v$) diagrams to constrain the velocity ranges of H I clouds that physically interact with the SNRs. The velocity channel maps provide a spatial correspondence between the SNR shell boundary and H I clouds as tested by previous studies (e.g. [Moriguchi et al. 2005](#)). When the H I clouds are associated with the SNR, they are expected to be located along with the shell. Likewise, H I cavities in $p - v$ diagrams are also expected when supernova shocks and/or stellar winds from the progenitor evacuated (accelerated) the H I gas.

In order to define the shock-interacting velocity range of H I clouds, we first prepared velocity channel maps of H I towards each SNR candidate. Because the shock-interacting clouds will be limb-brightened in the synchrotron radio continuum through the shock-cloud interactions with the magnetic field amplification, the velocity channel distribution of H I is useful to identify the spatial correlation between the shocked H I clouds and SNR candidate shells.

¹ To distinguish between SNR candidates and confirmed SNRs, [Maggi et al. \(2016\)](#) established nomenclature where bona fide Magellanic Clouds (MCs) SNRs are named with the prefix ‘MCSNR J’ and candidates with only ‘J’.

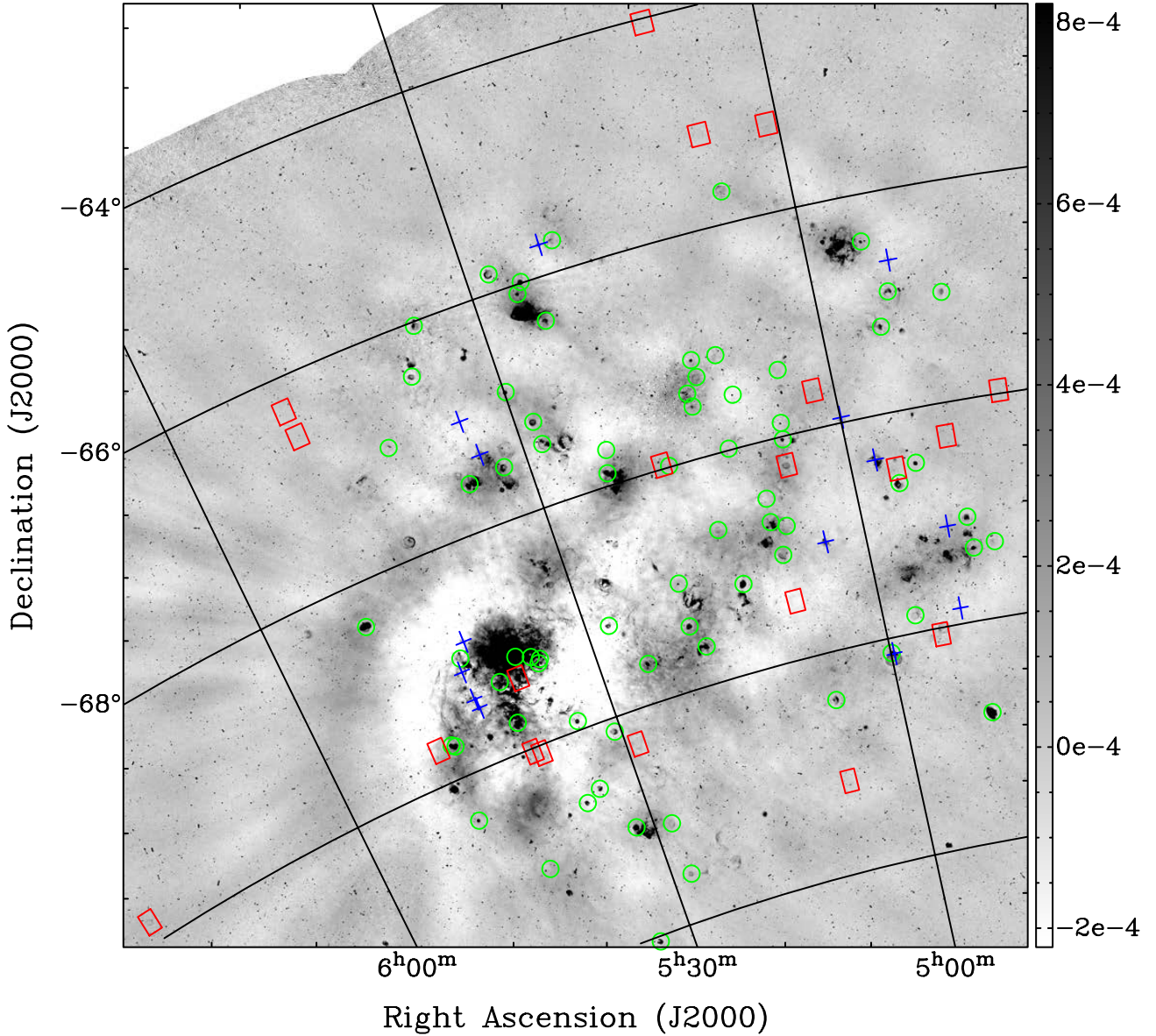


Figure 1. 14 new SNR candidate positions in the LMC are marked in blue crosses while 71 green circles represent known SNRs and 20 red rectangles are previously established SNR candidates. The background image is from the ASKAP survey of the LMC and the scale bar on the right hand side shows the surface brightness intensity scale in Jy beam^{-1} .

Here, we prepared a velocity channel distribution of H α as a velocity step of 6.6 km s^{-1} (see Appendix A). The map was centred at each SNR candidate with a size of $\sim 50 \times 50 \text{ arcmin}^2$. Finally, we searched for expanding shell-like structures in the $p - v$ diagram by changing the integration range of R.A. When the expanding gas motion is identified, we selected the H α velocity range which traces the inner edge of the cavity in the $p - v$ diagram.

3 RESULTS & DISCUSSION

The first extragalactic SNR was discovered over half a century ago as the LMC SNR N 49 (Mathewson & Healey 1963). Ever since then, studies of our Milky Way (MW) immediate neighbouring galaxy the LMC SNR sample is recognised as of essential importance because

it provides the best opportunity to reach a complete sample of these objects. With every new generation of astronomical instruments, we improved our knowledge about these objects as they come in large varieties. One of the most important aspects of these previous studies is to detect new SNRs which in return provides a better view of their evolutionary processes in various environments and with different progenitors.

As introduced in Section 1, we divide the LMC SNR population into two groups: bona fide SNRs and SNR candidates. Previous studies of the LMC SNRs revealed 71 confirmed objects (58+1+1+1+3+7 as in Bozzetto et al. 2017; Maggi et al. 2016; Maitra et al. 2019, 2021; Yew et al. 2021; Kavanagh et al. 2022) and 20 candidates (4+15+1 as in Bozzetto et al. 2017; Yew et al. 2021; Filipović et al. 2022). These studies are mainly based on the previous generation of ATCA radio, *XMM-Newton* and *Chandra X-*

ray and MCELS optical surveys. One of the main conclusions from [Bozzetto et al. \(2017\)](#) study of the LMC SNR sample is that we were missing detection of large size but low surface brightness SNRs. It was also acknowledged that some SNRs could escape detection as they could be embedded into the large scale HII regions such as 30 Doradus ([Kavanagh et al. 2015](#)). Along that expectation, we endeavour in a search for new LMC SNRs using the latest generation of ASKAP radio survey ([Pennock et al. 2021](#)).

3.1 Previous LMC SNR candidates

We first investigate the present LMC SNR candidate sample of 20 objects. [Yew et al. \(2021\)](#) found that none of their 15 optically selected candidates can be detected in our ASKAP survey. In addition to these, [Filipović et al. \(2022\)](#) suggested that ASKAP J0624–6948 is an intergalactic SNR positioned in the outskirts of the LMC, but the true nature of this object remains mysterious.

This leaves four remaining LMC SNR candidates that are initially investigated in [Bozzetto et al. \(2017\)](#): J0506–6815 ([HP99] 635), J0507–7110 (DEML81), J0538–6921 (MC 73) and J0539–7001 ([HP99] 1063)). We search for their radio continuum SNR signature in our ASKAP survey (see Fig. 2) as well as in other wavelengths.

We find that J0506–6815 ([HP99] 635) is a circular source in our ASKAP radio image (see Figs. 2 (top left panel) and 3) with an estimated flux densities of $S_{888\text{ MHz}}=78\pm 2$ mJy and $S_{1377\text{ MHz}}=64\pm 4$ mJy (from [Filipović et al. \(2021\)](#)) produce a spectral index $\alpha = -0.45 \pm 0.24$. Together with a prominent central soft X-ray emission in the *XMM-Newton* survey and $[S_{\text{II}}]/H\alpha > 0.9$, we now safely confirm MCSNR J0506–6815 as a bona fide SNR. Interestingly, the X-ray emission occupies central part of the SNR while radio and optical emission dominates at the edges. This anti-correlation indicates that MCSNR J0506–6815 could be very similar to the known iron-rich cores SNRs such as MCSNR J0506–7025 and MCSNR J0527–7104 ([Kavanagh et al. 2016, 2022](#)).

SNR candidate J0507–7110 (DEML81; Fig. 2 top right panel) shows some typical SNR morphological characteristics, but in our ASKAP LMC radio image this object is confused by the nearby emission and other sources. Therefore, we are keeping its status as a candidate SNR.

J0538–6921 (MC 73; Fig. 2 bottom left panel) is certainly a prototype radio SNR candidate based on its radio properties ($S_{888\text{ MHz}}=294\pm 3$ mJy; $S_{1377\text{ MHz}}=248\pm 4$ mJy; $S_{4800\text{ MHz}}=120\pm 10$ mJy; $\alpha = -0.56 \pm 0.02$) but lack of X-ray or optical confirmation prevent us from a final classification.

We clearly see a point radio source close to the centre of X-ray LMC SNR candidate J0539–7001 ([HP99] 1063; Fig. 2 bottom right panel), but we cannot confirm its SNR nature as the positional displacement between radio and X-ray position of ~ 25 arcsec is not negligible. Also, no other nearby and obvious fine-scale structure could be linked with the object’s possible SNR nature. However, we acknowledge that a compact type of SNR candidate such as J051327–6911 ([Bojčić et al. 2007](#)) is still a possibility.

3.2 New ASKAP LMC SNR candidates

We searched our new ASKAP images of the LMC for circular shaped objects (above 5σ of local noise) with an enhanced ratio of radio continuum to H α emission. This method, introduced by [Ye et al. \(1991\)](#), successfully identifies objects in which non-thermal emission is dominant, i.e. SNRs. Using this enhanced ratio,

combined with the typically circular SNR morphology, we find 14 regions in which the presence of an SNR is plausible. We present a catalogue of radio images of these newly discovered SNR candidates in Fig. 4 and details in Appendix A.

We used the method described in [Hurley-Walker et al. \(2019, Section 2.4\)](#) and [Filipović et al. \(2022\)](#) to measure the position, extent and flux densities of all 14 selected LMC SNR candidates. In the same manner, we measure the three ATCA observations of MCSNR J0522–6543 (at 2100, 5500 and 9000 MHz). In short, we carefully selected proposed SNR regions that exclude all obvious point sources and then measured the total radio flux density, accounting for local background. We note the selected SNR candidates have low surface brightness and/or are sometimes embedded in complex environments (c.f. J0457–6823, J0459–7008b² and J0459–6757). This significantly influences the accuracy or may prevent any meaningful measurements. We estimate our flux density measurements have an error of < 20 per cent. Also, [Filipović et al. \(2022, see their Figure 7\)](#) noted that a lack of short spacing data in observations³ may result in under-estimates of extended flux density measurements. [Filipović et al. \(2022\)](#) suggest that spectral index estimates could be as much as $\sim 15\text{--}20\%$ (or $\alpha \sim 0.1$) flatter.

In Table 1 we list the source name in Column 1, its central position (RA and DEC) in Columns 2 and 3, source angular extent as major and minor axis/diameter in Column 4 (in arcsec), arithmetic average of major and minor axes/diameter converted to parsecs for a distance of 50 kpc in Column 5, and position angle (PA) in Column 6, measured from north to east. Our flux density estimates at 888 MHz are listed in Column 7. As none of the here selected LMC SNR candidates (except for MCSNR J0522–6543) can be seen at other radio frequencies, we can not estimate their spectral index. To compare the surface brightness of our sample with established LMC SNRs, we assumed a typical SNR spectral index of $\alpha = -0.5$ ([Reynolds et al. 2012](#); [Galvin & Filipovic 2014](#); [Bozzetto et al. 2017](#); [Maggi et al. 2019](#); [Filipović & Tothill 2021b](#)). However, we acknowledge that some of our SNR candidates may contain an old PWN which would have a somewhat flatter spectral index. Using this assumed spectral index allowed us to estimate the flux density and surface brightness of these sources at 1 GHz (Column 8; $\Sigma_{1\text{ GHz}}$). In Column 9 we provide the number of massive OB stars found within a ~ 100 pc radius of each of the objects’ central position. Lastly, in Columns 10 and 11, Y/N apply when optical and X-ray data are available and/or the source is detected.

These 14 new SNR candidates escaped previous detection because of their low surface brightness, which indicates an advanced age. They are most likely evolved and expanding in a rarefied environment, and we note that they occupy the bottom part of the SNR Σ –D diagram ([Pavlović et al. 2018](#); [Urošević 2020](#)). In fact, the arithmetic average of surface brightness ($\Sigma_{1\text{ GHz}}$; Table 1, Column 8) from the sample of 40 LMC SNRs ([Bozzetto et al. 2017](#)) is $7.9 \times 10^{-21} \text{ W m}^{-2} \text{ Hz}^{-1} \text{ sr}^{-1}$ while from our sample of 14 new candidates is $4.5 \times 10^{-22} \text{ W m}^{-2} \text{ Hz}^{-1} \text{ sr}^{-1}$. This order of magnitude difference suggests that we are discovering low surface brightness SNRs in the LMC. At the same time, our sample SNR candidate diameters are fractionally larger but because of the large overlap with the sample of established LMC SNRs ($D_{\text{av}14\text{SNR}}=51.2$ pc and

² Because of the close proximity (and similar position) to SNR N186D, we use ‘b’ (as J0459–7008b) to distinguish between two possibly separate objects.

³ We also used the same 888 MHz image and the same ATCA array observations with the similar integration time.

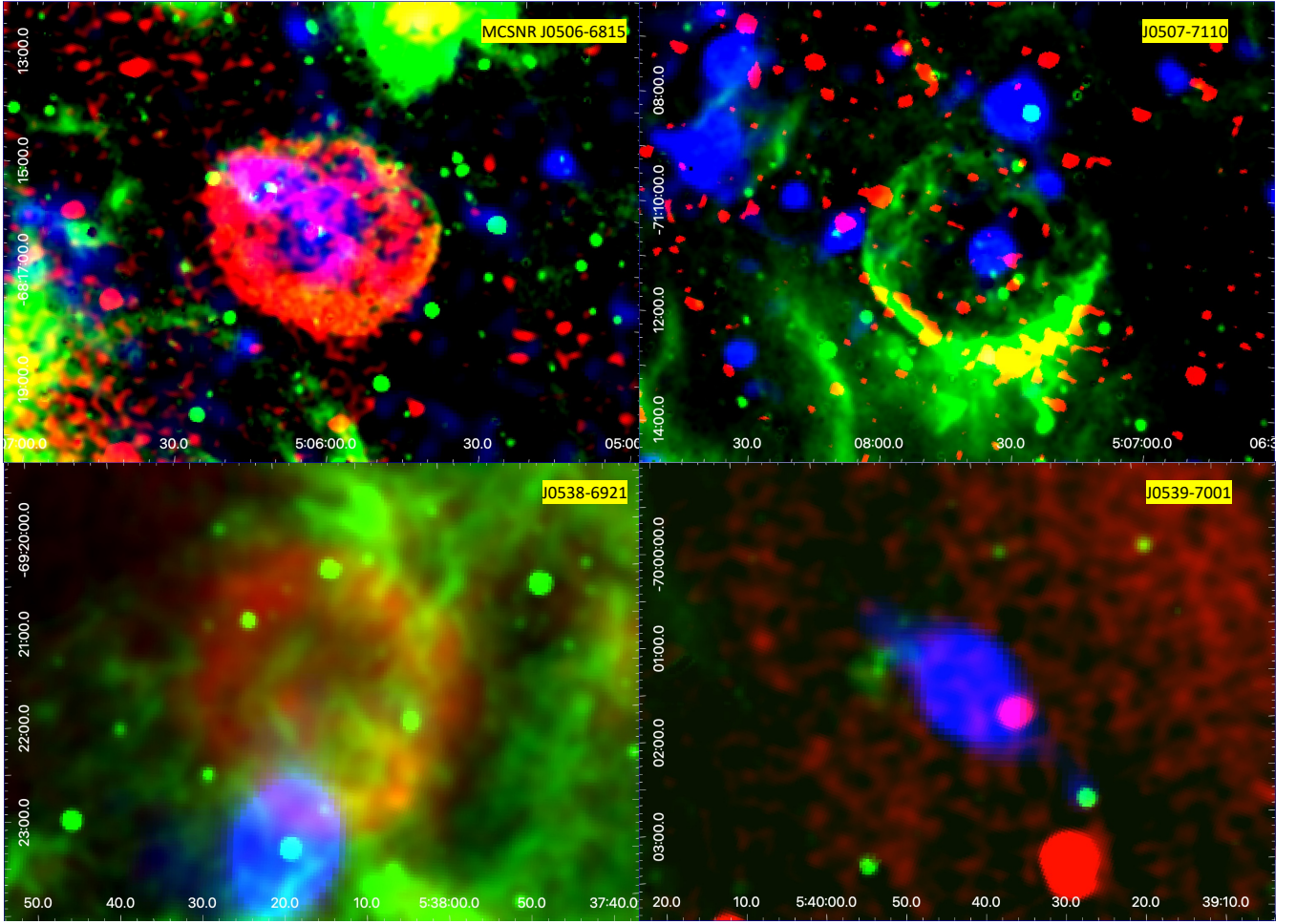


Figure 2. Previously selected LMC SNR candidates MCSNR J0506–6815 (top left), J0507–7110 (top right), J0538–6921 (bottom left) and J0539–7001 (bottom right). All RGB images made from the ASKAP 888 MHz radio data are in red (at 13.9×12.1 arcsec² resolution), H α in green and *XMM-Newton* 0.2–1.0 keV in blue. The previously selected SNR candidate, J0506–6815, is confirmed as a bona fide LMC SNR.

Table 1. The main properties of the 14 new LMC SNR candidates found in this study. The positional accuracy measurements are better than 2 arcsec while flux density errors are <20 per cent. † indicates that J0522–6543 is confirmed SNR in this study.

Name	RA (J2000) (h m s)	DEC (J2000) (° ′ ″)	$\theta_{\text{maj}} \times \theta_{\text{min}}$ (arcsec)	D_{av} (pc)	PA (°)	$S_{888 \text{ MHz}}$ (mJy)	$\Sigma_{1 \text{ GHz}}$ ($\text{W m}^{-2} \text{ Hz}^{-1} \text{ sr}^{-1} \times 10^{-22}$)	# OB Star Candidates	Optical ID	X-ray ID
J0451–6906	04 51 38.9	–69 06 26	299 × 194	58	90	27	2.41	19	Y	–
J0451–6951	04 51 50.8	–69 51 30	170 × 168	41	0	1	0.21	10	N	N
J0452–6638	04 52 42.4	–66 38 35	277 × 196	56	90	5	0.04	29	Y	–
J0457–6823	04 57 30.9	–68 23 35	196 × 115	36	60	—	—	33	Y	?
J0459–7008b	04 59 38.7	–70 08 37	203 × 178	46	150	—	—	44	Y	–
J0459–6757	04 59 54.9	–67 57 04	131 × 114	30	0	—	—	18	Y	–
J0504–6901	05 04 04.8	–69 01 12	259 × 246	61	22	93	7.49	72	Y	?
J0522–6543†	05 22 53.5	–65 43 09	171 × 159	40	0	35	6.54	15	Y	–
J0534–6720	05 34 05.5	–67 20 48	293 × 288	70	0	102	6.15	45	N	–
J0534–6700	05 34 48.7	–67 00 01	188 × 179	45	0	1	0.21	325	N	–
J0542–6852	05 42 05.9	–68 52 14	251 × 218	57	75	74	6.92	40	Y	Y
J0543–6928	05 43 06.3	–69 28 42	157 × 104	31	125	45	14.11	34	N	N
J0543–6923	05 43 16.5	–69 23 27	228 × 213	54	0	28	2.92	31	?	N
J0543–6906	05 43 25.2	–69 07 19	443 × 354	96	0	83	2.42	50	N	?

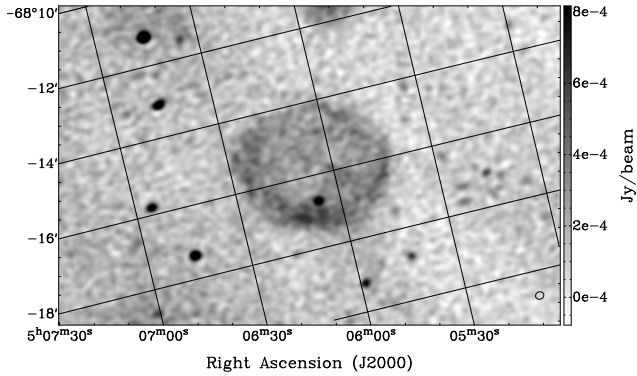


Figure 3. ASKAP image of MCSNR J0506–6815 with a beam size of 13.9×12.1 arcsec² (bottom right corner). We note unrelated point source towards the southern edges of the SNR.

SD=16.9 vs. $D_{av71SNR}=44.9$ pc and SD=24.9) we can not separate two samples.

The size distribution of the 14 new SNR candidates against the 71 (58+1+1+1+3+7) previously confirmed SNRs from [Bozzetto et al. \(2017\)](#), [Maggi et al. \(2016\)](#); [Maitra et al. \(2019, 2021\)](#), [Yew et al. \(2021\)](#) and [Kavanagh et al. \(2022\)](#) can be seen in Fig. 5. Our new sample of 14 LMC SNR candidates are distributed across a large range of sizes from ~ 30 to ~ 96 pc. From the sample of 71 known LMC SNRs, 45 objects have an estimated age, which spreads from the small size SN1987A of 35 yrs to the large 107 pc DEM L72 of 115000 yrs ([Klimek et al. 2010](#)), [Bozzetto et al. \(2017](#), see their fig. 18) showed that at age of ~ 5000 yrs SNRs such as N 49 ([Park et al. 2012](#)) or 30 Dor B (a.k.a. N 157B; [Chen et al. 2006](#)) can reach sizes of >30 pc in diameter which is mid-to-late Sedov phase. However, this is very much dependent on various factors such as the environmental density, initial progenitor type and its explosion energy. Nevertheless, this implies that our sample of 14 new objects belongs to a more evolved and mid-to-older (> 5000 yrs) SNR population.

We also cross-matched various X-ray surveys and pointed observations including *XMM-Newton* and *Chandra*. However, one would not expect to detect X-ray emission from an SNR in the very late stage of evolution in such a rarefied environment, especially at the distance of 50 kpc, as shown in the above-mentioned case of J0624–6948 ([Filipović et al. 2022](#)). SNR X-ray emission depends on ISM density squared, while synchrotron emission scales linearly with ISM density ([Duric 2000a,b](#); [Urošević 2022](#)). This implies that X-ray emission in less dense environments will fade much quicker than predominantly non-thermal (synchrotron) radio emission. In some cases (8/14) we can detect very weak optical emission (mainly $H\alpha$) which indicates active non-radiative shocks from the late Sedov and radiative phases, implying an older SNR.

Optical emission from SNRs typically originate from highly compressed, thin, radiative shells. This may further indicate the eight optically-identified SNR candidates are not expanding in a low-density medium. In 6 candidates, we did not detect optical emission, which suggests that these SNR candidates are in the radiative phase of their evolution. However, in the radiative phase, there could be significant emission from various coolants, depending on temperature (T). Most notably, we may see [OIII] emission from $T \sim 10^5$ K gas, as the X-ray emission of such shocks fades.

However, for $T \sim 10^5$ K there is little line emission in the MCELS optical bands that we use here. This all implies that in many cases, the X-rays from SNRs fade first followed by the optical emission and then the last standing emission before the remnant completely disappears would come from radio continuum ([Vink 2020](#)). That suggests, the eight optically-detected candidates are perhaps not as old as those in which we detect only radio emission. We also detect one SNR candidate (J0542–6852) in the *XMM-Newton* survey which strengthens our SNR classification for this source.

We investigate the H α properties of our SNR candidate sample (see Appendix A). As a result, $\sim 80\%$ (11 out of 14) of them show possible evidence of expanding H α shells, which were likely formed by a combination of shock waves and strong stellar winds from the massive progenitor (and possibly surrounding OB stars). As shown in the Appendix A, several SNRs show a good spatial correspondence between the intensity peaks of the radio continuum and H α , suggesting that shock-cloud interactions occurred. Indeed, our $p - v$ diagrams show cavities in which these SNRs are almost freely expanding ([Sano et al. 2020](#); [Luken et al. 2020](#); [Alsaberi et al. 2019](#)). Some of these 14 LMC SNR candidates (such as J0451–6906, J0457–6823, J0459–6757, J0534–6720, J0534–6700, J0542–6852 and J0543–6923) have reached the wind-cavity of H α , while others (such as J0452–6638, J0504–6901, J0522–6543) are in the free expansion phase inside the wind bubble. This is very similar to Galactic SNRs SN 1006 ([Sano et al. 2022](#)), G346.6–0.2 ([Sano et al. 2021b](#)) and the mixed-morphology W49B ([Sano et al. 2021a](#)) where a wind-blown bubble was found along the radio continuum shell with an expansion velocity of ~ 10 km s⁻¹, which was likely formed by strong stellar winds from the high-mass progenitor of the SNR.

Finally, we investigate the stellar environment of each of our 14 SNR candidates (Fig. 6) using a 100 pc ($\sim 10^7$ yr at 10 km s⁻¹) search radius. The number of OB stars (N_{OB}) in the environments of these objects is an indicator of whether they are more likely to be core-collapse rather than type Ia SNRs, as such short-lived stars are a direct tracers of star formation activity that must have occurred recently in the core-collapse scenario. This indicator was calibrated in the LMC in [Maggi et al. \(2016\)](#) using SNR types determined via other methods. Numbers of neighbouring OB stars less than 15 are associated with type Ia SNRs while CC SNRs had generally (much) more than 35 such stars around them. The overall number of OB stars in our candidates trend toward the lower end of what is observed in other confirmed LMC SNRs with several in the ‘undecided’ range. The outlier here is J0534–6700 which has 325 blue early-type stars in the immediate vicinity of the remnant which point toward a most likely core-collapse scenario. However, in the SNR-cavities we also expect a small number of neighbouring OB stars which suggests relatively low-mass (8–10 M_{\odot}) SN II-P progenitors. The local ratio of red supergiants to OB stars might corroborate such a hypothesis as well.

4 CONCLUSIONS

We have presented 14 new SNR candidates in the LMC, adding to the ongoing effort of compiling a comprehensive set of LMC SNRs. For one of these 14 objects (MCSNR J0522–6543) we confirm SNR nature based on the elevated [SII]/ $H\alpha$ ratio and non-thermal radio spectral index (see Appendix A8) as well as for one previously selected candidate (MCSNR J0506–6815). This increases the count of SNRs in the LMC to 73 confirmed and 32 candidates. Our radio candidates are fainter in comparison to previously known SNRs in

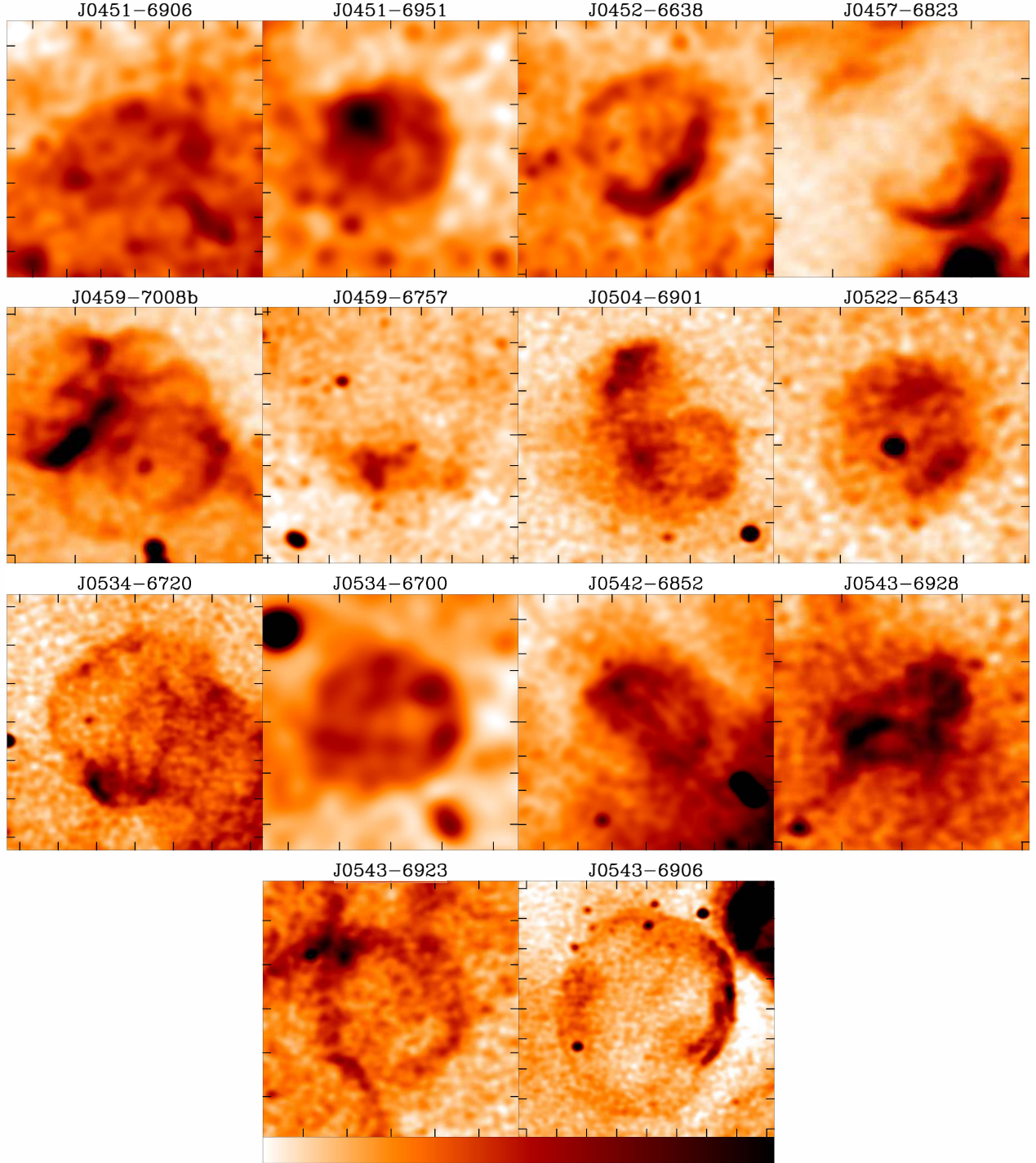


Figure 4. ASKAP radio images of all 14 newly discovered LMC SNRs candidates centred at the locations indicated in Table 1. Tick intervals of 1 arcmin correspond to 14.5 pc at the distance of the LMC. The images for SNR candidates J0459-6757 and J0542-6852 have been convolved to 20 arcsec, those of SNR candidates J0451-6906, J0451-6951, J0452-6638 and J0534-6700 to 30 arcsec in order to enhance the signal-to-noise ratio of low surface brightness sources. The colour bar for all images is shown at the bottom of the panel. The intensity ranges in mJy/beams for the 14 panels are from top left to bottom right are: $(-0.2 : 1.6)$ $(-0.8 : 0.5)$ $(-0.8 : 1.1)$ $(-0.2 : 3.3)$ $(-0.2 : 2.5)$ $(-0.2 : 1.7)$ $(-0.2 : 1.5)$ $(-0.2 : 1.2)$ $(-0.2 : 1.2)$ $(-1.1 : 0.6)$ $(-1.4 : 1.2)$ $(-0.4 : 1.0)$ $(-0.4 : 1.0)$ $(-0.3 : 1.5)$. We note that J0522-6543 is confirmed SNR in this study.

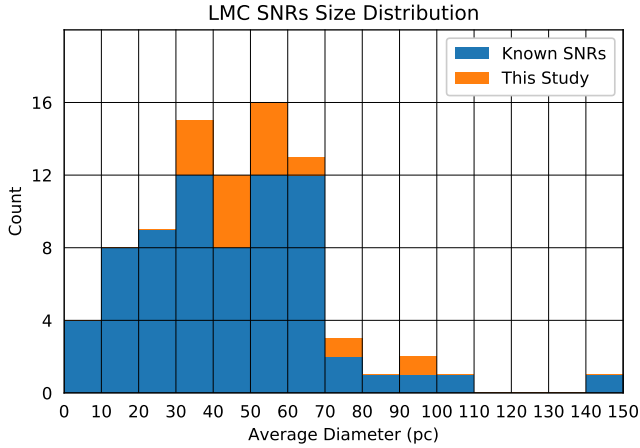


Figure 5. The distribution of 14 new LMC SNR candidate diameters (orange) added to the 71 previously known (blue). These 71 confirmed SNRs are detected in (Bozzetto et al. 2017; Maggi et al. 2016; Maitra et al. 2019, 2021; Yew et al. 2021; Kavanagh et al. 2022).

the LMC; their detection made possible by a new generation of radio telescopes with improved sensitivity (such as ASKAP). Most of our candidate remnants do not have counterparts in the X-ray domain because of the non-complete coverage and poor sensitivity, but a few have optical signatures. These SNR candidates have a low surface brightness compared to their diameter, which we interpret as indicating an evolution in a rarefied medium. This conclusion is supported by their predominantly circular morphology. We suggest a few of these remnant candidates may have a SN type Ia origin (fewer OB stars than commonly seen) while others may be expanding in a cavity resulting from previous winds or SNe. Future work using deeper radio observations (at multiple wavelengths to allow the calculation of spectral indices and confirmation of their non-thermal nature) and deeper targeted X-ray and optical observations will be essential in confirming these sources as SNRs.

ACKNOWLEDGEMENTS

The Australian SKA Pathfinder is part of the Australia Telescope National Facility which is managed by Australian Commonwealth Scientific and Industrial Research Organisation (CSIRO). Operation of ASKAP is funded by the Australian Government with support from the National Collaborative Research Infrastructure Strategy. ASKAP uses the resources of the Pawsey Supercomputing Centre. Establishment of ASKAP, the Murchison Radio-astronomy Observatory and the Pawsey Supercomputing Centre are initiatives of the Australian Government, with support from the Government of Western Australia and the Science and Industry Endowment Fund. We acknowledge the Wajarri Yamatji people as the traditional owners of the Observatory site. This work was supported by resources provided by the Pawsey Supercomputing Centre with funding from the Australian Government and the Government of Western Australia. D.U. acknowledges the Ministry of Education, Science and Technological Development of the Republic of Serbia through contract No. 451-03-68/2022-14/200104, and for support through the joint project of the Serbian Academy of Sciences and Arts and Bulgarian Academy of Sciences on the detection of extragalactic SNRs and HI regions. MS acknowledges support from the Deutsche Forschungs-

gemeinschaft through the grants SA 2131/13-1, SA 2131/14-1, and SA 2131/15-1. We thank the anonymous referee for comments and suggestions that greatly improved our paper.

DATA AVAILABILITY

The data that support the plots/images within this paper and other findings of this study are available from the corresponding author upon reasonable request. The ASKAP data used in this article are available through the CSIRO ASKAP Science Data Archive (CASDA) and ATCA data via the Australia Telescope Online Archive (ATOA).

REFERENCES

- Alsaberi R. Z. E., et al., 2019, *Ap&SS*, **364**, 204
 Bojičić I. S., Filipović M. D., Parker Q. A., Payne J. L., Jones P. A., Reid W., Kawamura A., Fukui Y., 2007, *MNRAS*, **378**, 1237
 Bozzetto L. M., et al., 2017, *ApJS*, **230**, 2
 Chen Y., Wang Q. D., Gotthelf E. V., Jiang B., Chu Y.-H., Gruendl R., 2006, *ApJ*, **651**, 237
 Davies R. D., Elliott K. H., Meaburn J., 1976, *Mem. RAS*, **81**, 89
 Duric N., 2000a, in Berkhuijsen E. M., Beck R., Walterbos R. A. M., eds, Proceedings 232. WE-Heraeus Seminar. pp 127–130
 Duric N., 2000b, in Berkhuijsen E. M., Beck R., Walterbos R. A. M., eds, Proceedings 232. WE-Heraeus Seminar. pp 179–186
 Filipović M. D., Tothill N. F. H., eds, 2021b, *Multimessenger Astronomy in Practice*. 2514-3433, IOP Publishing, doi:10.1088/2514-3433/ac2256, https://dx.doi.org/10.1088/2514-3433/ac2256
 Filipović M. D., Tothill N. F. H., 2021a, *Principles of Multimessenger Astronomy*. AAS-IOP astronomy, Institute of Physics Publishing, doi:10.1088/2514-3433/ac087e
 Filipovic M. D., Haynes R. F., White G. L., Jones P. A., Klein U., Wielebinski R., 1995, *A&AS*, **111**, 311
 Filipovic M. D., White G. L., Haynes R. F., Jones P. A., Meinert D., Wielebinski R., Klein U., 1996, *A&AS*, **120**, 77
 Filipovic M. D., Haynes R. F., White G. L., Jones P. A., 1998, *A&AS*, **130**, 421
 Filipović M. D., et al., 2021, *MNRAS*, **507**, 2885
 Filipović M. D., et al., 2022, *MNRAS*, **512**, 265
 Galvin T. J., Filipovic M. D., 2014, *Serbian Astronomical Journal*, **189**, 15
 Haberl F., 2019, in *A Synoptic View of the Magellanic Clouds: VMC, Gaia and Beyond*. p. 63, doi:10.5281/zenodo.3472583
 Haberl F., Pietsch W., 1999, *A&AS*, **139**, 277
 Hurley-Walker N., et al., 2019, *Publ. Astron. Soc. Australia*, **36**, e048
 Hurley-Walker N., Payne J. L., Filipović M. D., Tothill N., 2021, in Filipović M. D., Tothill N. F. H., eds, 2514-3433, *Multimessenger Astronomy in Practice*. IOP Publishing, pp 2–1, doi:10.1088/2514-3433/ac2256ch2
 Jaskot A. E., Strickland D. K., Oey M. S., Chu Y. H., García-Segura G., 2011, *ApJ*, **729**, 28
 Johnston S., et al., 2022, *MNRAS*, **509**, 5209
 Kavanagh P. J., Sasaki M., Bozzetto L. M., Filipović M. D., Points S. D., Maggi P., Haberl F., 2015, *A&A*, **573**, A73
 Kavanagh P. J., et al., 2016, *A&A*, **586**, A4
 Kavanagh P. J., Sasaki M., Filipović M. D., Points S. D., Bozzetto L. M., Haberl F., Maggi P., Maitra C., 2022, *MNRAS*,
 Kim S., Staveley-Smith L., Dopita M. A., Sauls R. J., Freeman K. C., Lee Y., Chu Y.-H., 2003, *ApJS*, **148**, 473
 Klimek M. D., Points S. D., Smith R. C., Shelton R. L., Williams R., 2010, *ApJ*, **725**, 2281
 Kontizas M., Morgan D. H., Hatzidimitriou D., Kontizas E., 1990, *A&AS*, **84**, 527
 Koribalski B. S., Norris R. P., Andernach H., Rudnick L., Shabala S., Filipović M., Lenc E., 2021, *MNRAS*, **505**, L11
 Leahy D. A., 2017, *ApJ*, **837**, 36

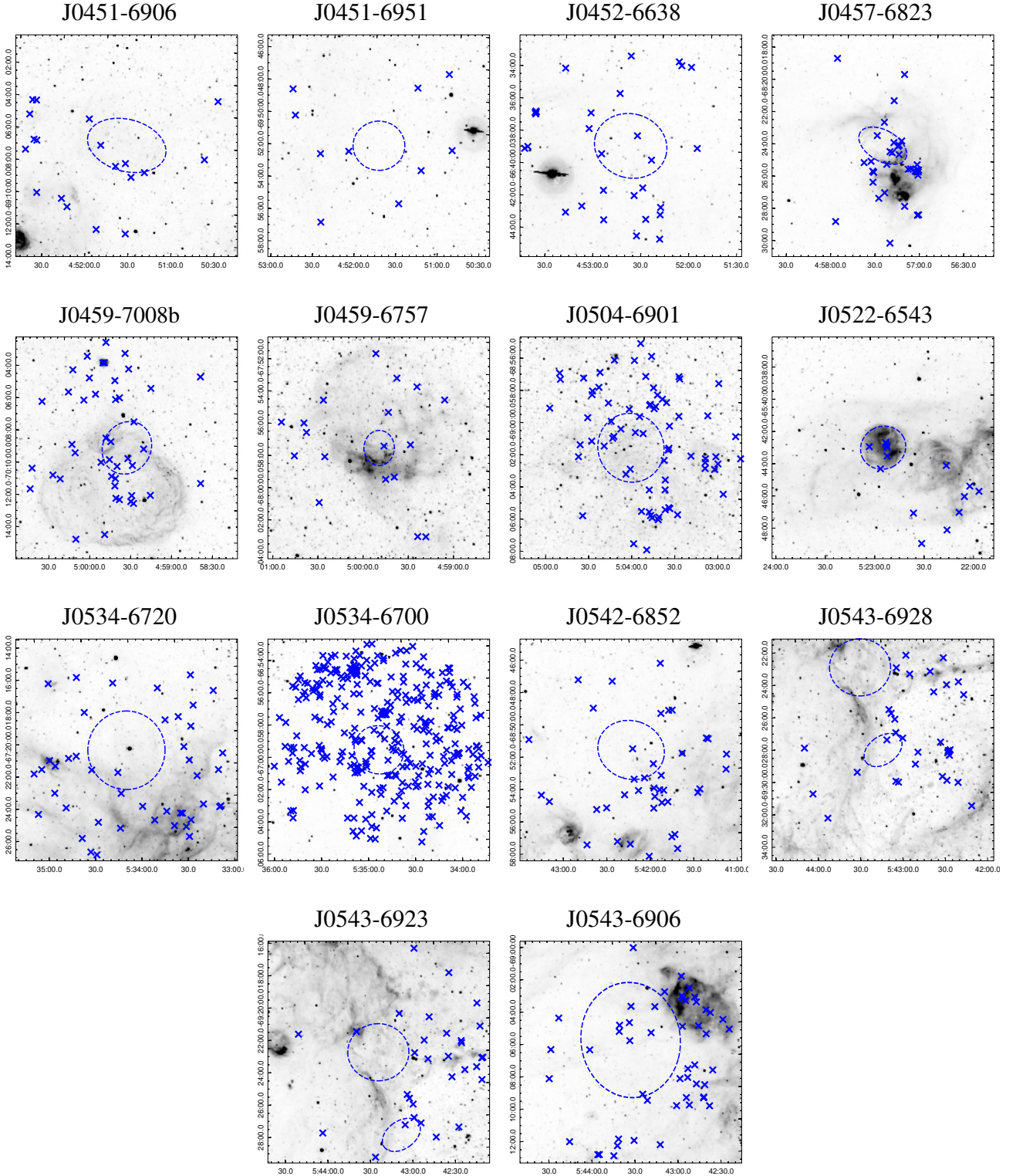


Figure 6. MCELS images (grey-scale) of the $H\alpha$ emission around 14 new SNR candidates in the LMC. The dashed ellipses indicate the measured extent of the SNR candidates (as per the data given in Table 1) and the crosses mark the positions of massive star (OB) candidates within 100 pc of the centre of the SNR candidates. We note that J0543–6928 and J0543–6923 are sufficiently close together to appear in the each other’s plot.

Leahy D. A., Ranasinghe S., Gelowitz M., 2020, *ApJS*, **248**, 16

Luken K. J., et al., 2020, *MNRAS*, **492**, 2606

Maggi P., 2021, in Filipović M. D., Tothill N. F. H., eds, 2514-3433, *Multimessenger Astronomy in Practice*. IOP Publishing, pp 6–1, doi:10.1088/2514-3433/ac2256ch6

Maggi P., et al., 2016, *A&A*, **585**, A162

Maggi P., et al., 2019, *A&A*, **631**, A127

Maitra C., et al., 2019, *MNRAS*, **490**, 5494

Maitra C., Haberl F., Maggi P., Kavanagh P. J., Vasilopoulos G., Sasaki M., Filipović M. D., Udalski A., 2021, *MNRAS*, **504**, 326

Mathewson D. S., Healey J. R., 1963, *Nature*, **199**, 681

Mathewson D. S., Healey J. R., 1964, in *Symposium International Astronomical Union; Kerr F. J., ed.*, Vol. 20, *The Galaxy and the Magellanic Clouds*. Cambridge University Press, p. 245

Meaburn J., 1980, *MNRAS*, **192**, 365

Meixner M., et al., 2006, *AJ*, **132**, 2268

Moriguchi Y., Tamura K., Tawara Y., Sasago H., Yamaoka K., Onishi T., Fukui Y., 2005, *ApJ*, **631**, 947

Norris R. P., et al., 2021, *Publ. Astron. Soc. Australia*, **38**, e003

Oey M. S., Groves B., Staveley-Smith L., Smith R. C., 2002, *AJ*, **123**, 255

Offringa A. R., McKinley B., Hurley-Walker et al., 2014, *MNRAS*, **444**, 606

Park S., Hughes J. P., Slane P. O., Burrows D. N., Lee J.-J., Mori K., 2012, *ApJ*, **748**, 117

Pavlović M. Z., Urošević D., Arbutina B., Orlando S., Maxted N., Filipović M. D., 2018, *ApJ*, **852**, 84

Pennock C. M., et al., 2021, *MNRAS*, **506**, 3540

Pietrzyński G., et al., 2019, *Nature*, **567**, 200

Points S. D., Long K. S., Winkler P. F., Blair W. P., 2019, *ApJ*, **887**, 66

Reynolds S. P., Gaensler B. M., Bocchino F., 2012, *Space Science Reviews*, **166**, 231

Sano H., et al., 2020, *ApJ*, **902**, 53

Sano H., et al., 2021a, *ApJ*, **919**, 123

Sano H., Suzuki H., Nobukawa K. K., Filipović M. D., Fukui Y., Moriya T. J., 2021b, *ApJ*, **923**, 15

Sano H., Yamaguchi H., Aruga M., Fukui Y., Tachihara K., Filipović M. D., Rowell G., 2022, *ApJ*, **933**, 157

Schneider F. R. N., et al., 2018, *Science*, **359**, 69

Urošević D., 2020, *Nature Astronomy*, **4**, 910

Urošević D., 2022, *PASP*, **134**, 061001

Uyaniker B., Reich W., Yar A., Kothes R., Fürst E., 2002, *A&A*, **389**, L61

Vink J., 2020, *Physics and Evolution of Supernova Remnants*, doi:10.1007/978-3-030-55231-2.

Ye T., Turtle A. J., Kennicutt R. C. J., 1991, *MNRAS*, **249**, 722

Yew M., et al., 2021, *MNRAS*, **500**, 2336

Zaritsky D., Harris J., Thompson I. B., Grebel E. K., 2004, *AJ*, **128**, 1606

⁵Max-Planck-Institut für extraterrestrische Physik, Gießenbachstraße 1, D-85748 Garching, Germany

⁶Australian Astronomical Optics, AAO-Macquarie, Faculty of Science and Engineering, Macquarie University, 105 Delhi Rd, North Ryde, NSW 2113, Australia

⁷INAF – Osservatorio Astrofisico di Catania, via Santa Sofia 78, I-95123 Catania, Italia

⁸The Inter-University Institute for Data Intensive Astronomy (IDIA), Department of Astronomy, University of Cape Town, Rondebosch 7701, South Africa

⁹School of Cosmic Physics, Dublin Institute for Advanced Studies, 31 Fitzwilliam Place, Dublin 2, Ireland

¹⁰ATNF, CSIRO Space & Astronomy, PO Box 76, Epping, NSW 1710, Australia

¹¹Dominion Radio Astrophysical Observatory, Herzberg Astronomy and Astrophysics, National Research Council Canada, PO Box 248, Penticton BC V2A 6J9, Canada

¹²Department of Physics and Astronomy, University of Calgary, University of Calgary, Calgary, Alberta, T2N 1N4, Canada

¹³Department of Physics, University of Crete, GR-70013 Heraklion, Greece; Institute of Astrophysics, FORTH, GR-71110 Heraklion, Greece

¹⁴Observatoire Astronomique de Strasbourg, Université de Strasbourg, CNRS, 11 rue de l'Université, F-67000 Strasbourg, France

¹⁵Lennard-Jones Laboratories, Keele University, Staffordshire ST5 5BG, UK

¹⁶Cerro Tololo Inter-American Observatory/NSF's NOIRLab, Casilla 603, La Serena, Chile

¹⁷Observatory Hill Waitoki, 130 Dormer Rd, Helensville RD2, Auckland 0875, New Zealand

¹⁸School of Mathematical and Physical Sciences, Macquarie University, Sydney, NSW 2109, Australia

¹⁹School of Physical Sciences, The University of Adelaide, Adelaide 5005, Australia

²⁰Dr. Karl Remeis Observatory, Erlangen Centre for Astroparticle Physics, Friedrich-Alexander-Universität Erlangen-Nürnberg, Sternwartstraße 7, 96049 Bamberg, Germany

²¹Department of Physics and Astronomy, University of Manitoba, Winnipeg, MB R3T 2N2, Canada

²²Department of Astronomy, Faculty of Mathematics, University of Belgrade, Studentski trg 16, 11000 Belgrade, Serbia

²³Isaac Newton Institute of Chile, Yugoslavia Branch

Please note: Oxford University Press is not responsible for the content or functionality of any supporting materials supplied by the authors. Any queries (other than missing material) should be directed to the corresponding author for the article.

¹Western Sydney University, Locked Bag 1797, Penrith South DC, NSW 2751, Australia

²Faculty of Engineering, Gifu University, 1-1 Yanagido, Gifu 501-1193, Japan

³Dublin Institute for Advanced Studies, Astronomy & Astrophysics Section, 31 Fitzwilliam Place, D02 XF86 Dublin 2, Ireland

⁴Center for Data Intensive and Time Domain Astronomy, Department of Physics and Astronomy, Michigan State University, East Lansing, MI 48824, USA

APPENDIX A: PROPERTIES OF 14 NEWLY DISCOVERED LMC SNR CANDIDATES

We present the properties of each LMC remnant candidate detected in this study such as their extent, radio morphology, potential OB associations and counterpart emission at other wavelengths.

A1 J0451–6906

The emission of this potential SNR from the ASKAP radio image appears as a faint shell morphology with slight rim brightening toward the western region (Figs. 4 and A1). The western rim of this emission also has elevated $[S_{11}]/H\alpha$ (>0.5), which helps push the case for the SNR candidate classification. Five of the 19 massive (OB) stars close to this candidate are positioned in the south/eastern rim of this tentative remnant. Its optical and radio boundaries are not obvious but our HI and $p - v$ diagram shows evidence of a cavity-like structure typical of a SNR expanding inside this cavity.

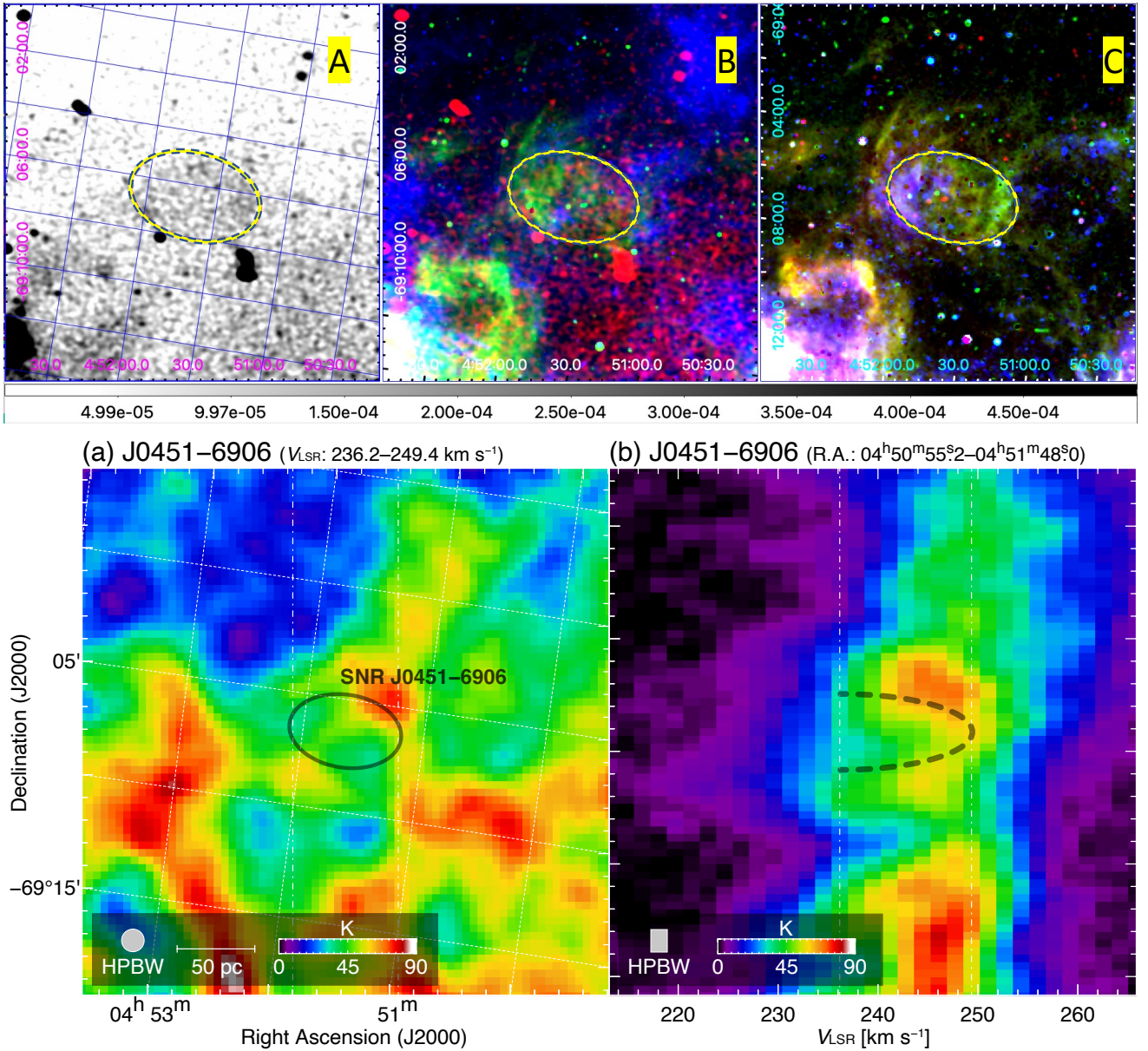


Figure A1. J0451–6906: (Top) Left (A): New ASKAP 888 MHz radio image at a spatial resolution of 13.9×12.1 arcsec 2 and position angle -84° . Gray scale at the bottom is from 0 to 0.5 mJy beam $^{-1}$. Middle (B): RGB image where ASKAP 888 MHz radio image is in red, H α (green) and Spitzer LMC-SAGE at $8\mu\text{m}$ in blue. Right (C): MCELS optical RGB image where H α (red), [SII] (green), & [OIII] (blue). (Bottom) Left (D): Integrated intensity map of HI obtained with ATCA & Parkes (Kim et al. 2003). The vertical dash-dotted (white) lines indicate the R.A. integration range for the position–velocity diagram. The blue–yellow ellipse indicates positions of here proposed SNR. Right (E): Position–velocity diagram of HI. The dashed curve delineates a cavity-like structure of HI. The vertical dash-dotted lines indicate the velocity integration range for the HI integrated intensity map.

A2 J0451–6951

This source exhibits a circular shell morphology (Fig. 4 and A2). Its diameter, $D = 41$ pc, is a typical size for the LMC SNRs sample (where the average is 44.9 pc). 10 OB star candidates are located within 100 pc of the source, but none are located within the measured extent of the candidate. No obvious optical or X-ray emission was found.

A3 J0452–6638

This SNR candidate exhibits a shell, which is brightest to the south and west (Figs. 4 and A3), with $D = 56$ pc and a very low surface brightness. Its radio emission coincides with the optical extent as it brightens on the south–west limb. There are 29 OB star candidates within 100 pc of the source, with four of these located within the extent of the ring emission. HI and $p - v$ diagram shows a cavity typical for SNRs (Sano et al. 2020; Luken et al. 2020; Alsaferi et al. 2019).

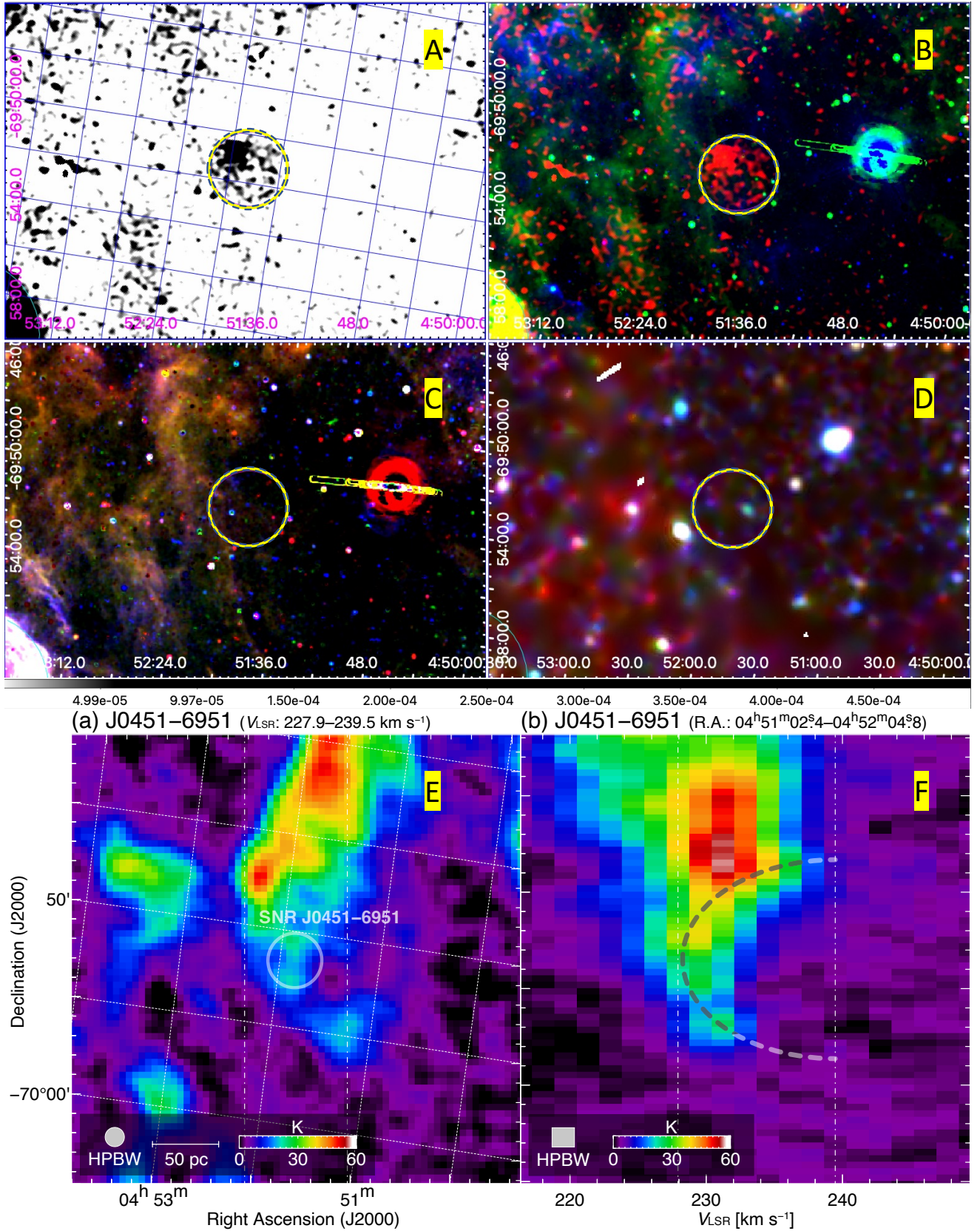


Figure A2. J0451–6951: (Top) Left (A): New ASKAP 888 MHz radio image at spatial resolution of 13.9×12.1 arcsec² and position angle -84° . Gray scale at the bottom is from 0 to $0.5 \text{ mJy beam}^{-1}$. Right (B): RGB image where ASKAP 888 MHz radio image is in red, $H\alpha$ (green) and Spitzer LMC-SAGE at $8\mu\text{m}$ in blue. (Middle) Left (C): MCELS optical RGB image where $H\alpha$ (red), $[\text{SII}]$ (green), & $[\text{OIII}]$ (blue). Right (D): *XMM-Newton* X-ray images using the soft (0.3–0.7 keV; red), medium (0.7–1.1 keV; green), and hard (1.1–4.2 keV; blue) bands. The blue-yellow ellipse indicates positions of here proposed SNR. (Bottom) Left (E): Integrated intensity map of H I obtained with ATCA & Parkes (Kim et al. 2003). Right (F): Position–velocity diagram of H I. We note image artefacts in the optical (B and C) and X-ray (D) panels which are caused by the removal of noisy pixels and by CCD chip gaps.

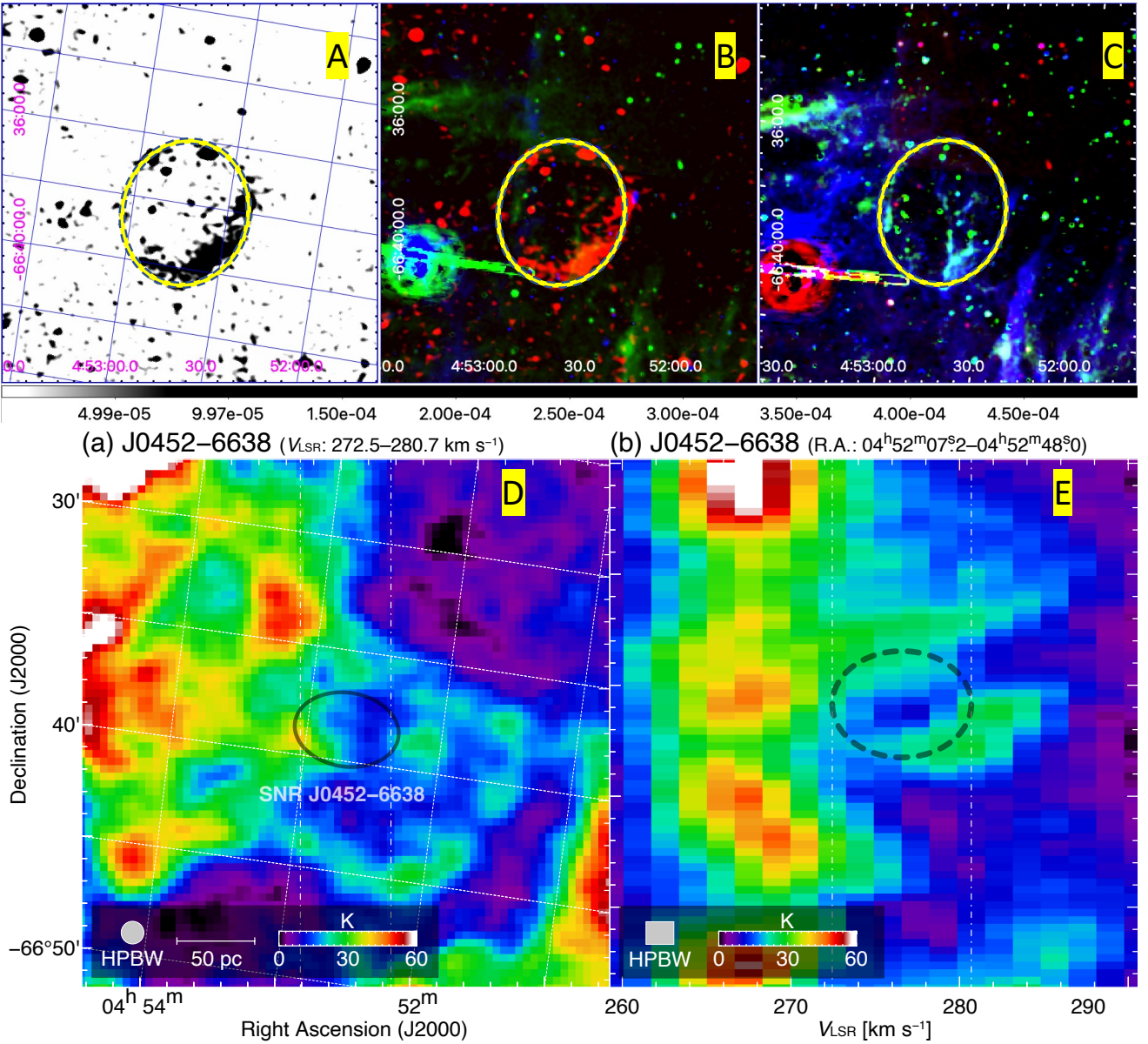


Figure A3. J0452-6638: Same as Fig. A1. We note image artefacts in the optical (B and C) panels.

A4 J0457-6823

This SNR candidate exhibits an elongated structure that can be seen best in the south-west where the source is possibly colliding, overlapping or embedded in emission from a separate nearby source (Figs. 4 and A4). A faint extended source at this position was detected at soft X-ray energies by Haberl & Pietsch (1999); source number 655 in their catalogue ([HP99] 655). The X-ray existence likelihood is low, due to the large off-axis angle of the source during the *ROSAT* observation and better data are needed to confirm any association with the SNR candidate. There are 33 OB star candidates located within, or in close proximity to this source – seven of the eight located inside the bounds of the remnant are located in the south-western region where there is higher radio emission. The HI map and $p - v$ diagram show the existence of a cavity but the $[\text{SiII}]/\text{H}\alpha$ ratio of 0.35 does not strongly favour an SNR. Therefore, we classify this object as a low confidence SNR candidate.

A5 J0459-7008b

The emission in this region is obfuscated by emission in the south from the massive superbubble N 186 (Oey et al. 2002). Located only 90 arcsec towards the east, the previously established MC-SNR J0459-7008 (a.k.a. N 186D) with a diameter of 34.3 pc (Jaskot et al. 2011) is indicated by a bright shell in the centre left of Fig. 4. There appears to be an almost circular ring of emission ($D=43$ pc) located to the west from the previously established SNR (Figs. 4 and A5). In addition, there are two more faint radio shells to the north and one to the south-east. The elevated $[\text{SiII}]/\text{H}\alpha (>0.7)$ and radio-to- $\text{H}\alpha$ levels also have a SNR shell-type morphology covering the same general area. In a search for massive stars in the region, we find 44 OB star candidates with ~ 6 within the projected bounds of the region. Also, the HI map and the $p - v$ diagram show a feature and possible cavity (see Fig. A5; Panel E). Finally, we note that SNR N 186D is very bright in $[\text{OIII}]$ while here proposed SNR candidate

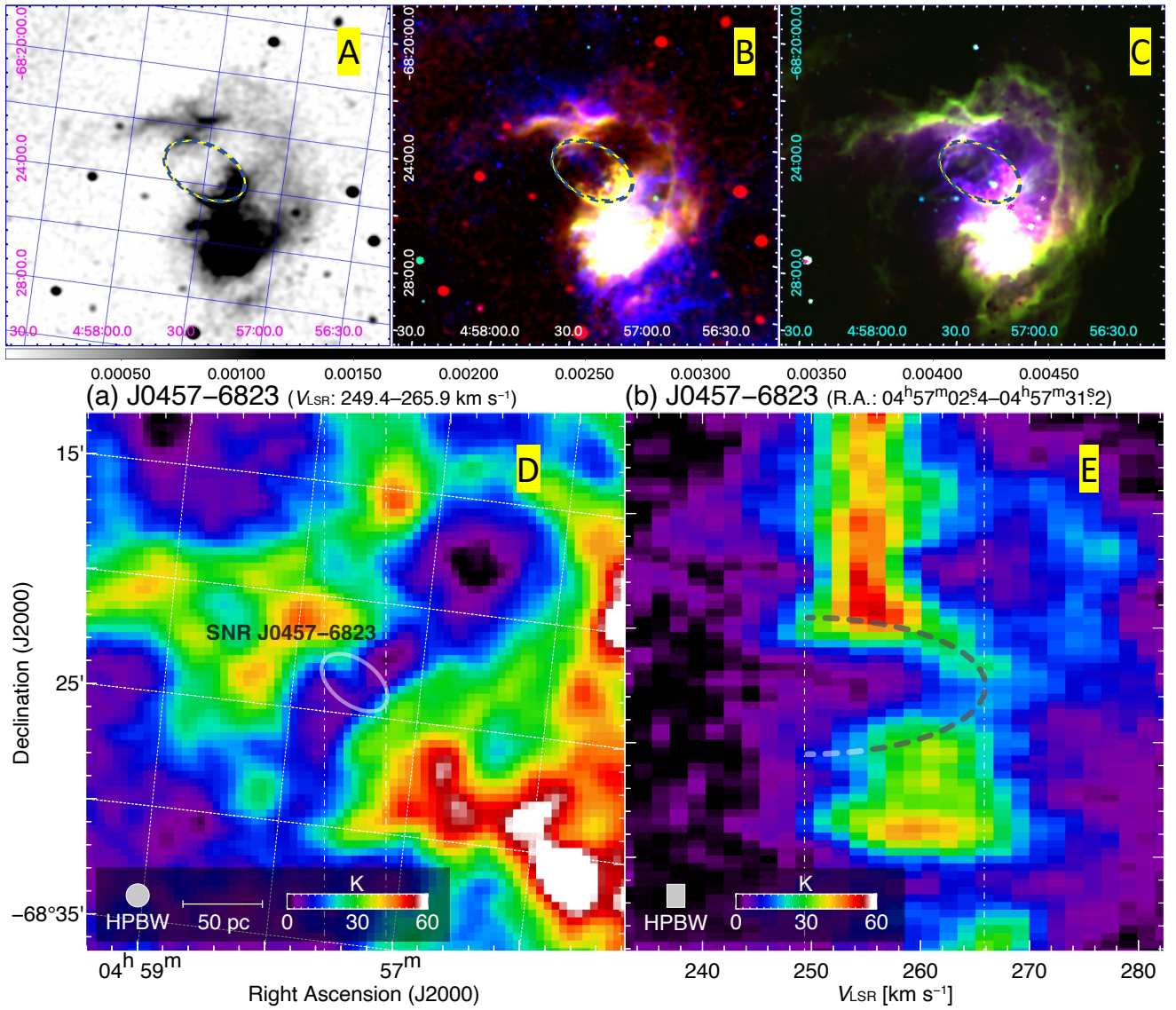


Figure A4. J0457–6823: Same as Fig. A1. Gray scale at the bottom of panel A (ASKAP image) is from 0 to 5 mJy beam⁻¹.

J0459–7008b is bright in [SII]. This is good indication that we see two different SNRs.

A6 J0459–6757

This is the smallest SNR candidate in our sample having a diameter of 30 pc embedded in the massive HII region N 16A. It has an elongated half-ring morphology, with the strongest emission seen toward the source’s southern boundary where it appears to be interacting with a gas cloud resulting in rim brightening (Figs. 4 and A6). While the radio-to-H α ratio is only mildly enhanced, the [SII]/H α ratio is not elevated indicating the absence of radiative shocks. This is a very tentative candidate with more evidence shown by its optical properties. There are 18 OB star candidates located within, or in close proximity to this source but only one within the projected bounds. Both HI map and $p - v$ diagram indicate the presence of a cavity, so we tentatively classify this object as SNR candidate.

A7 J0504–6901

J0504–6901 is a potential remnant of an SN that exhibits a complex and large ($D = 61$ pc) shell-morphology with a brightened region just off-centre and another in the northern part (Figs. 4 and A7). It is placed in the larger region known as DEM L64 and originally was detected as a radio source (LMC B0504–6906) in Filipovic et al. (1995, 1996, 1998) Parkes surveys. They found step spectral index of $\alpha = -1.2 \pm 0.4$ which supports a non-thermal radio spectrum, hence possible SNR identification. However, at least one strong nearby radio source (J0503–6903) and a number of other fainter ones are within the large Parkes beams (ranging from 2.7 arcmin at 8640 MHz to 15.2 arcmin at 1400 MHz) and would significantly contribute the measured flux densities and therefore may not represent the true spectral index of this LMC source alone. Very strong elevation of the radio-to-H α ratio warrants the SNR candidate classification even though no clear X-ray (due to a low exposure time and a large off-axis angle) or optical boundaries could be drawn. There are 72 OB star candidates located within, or in close proxim-

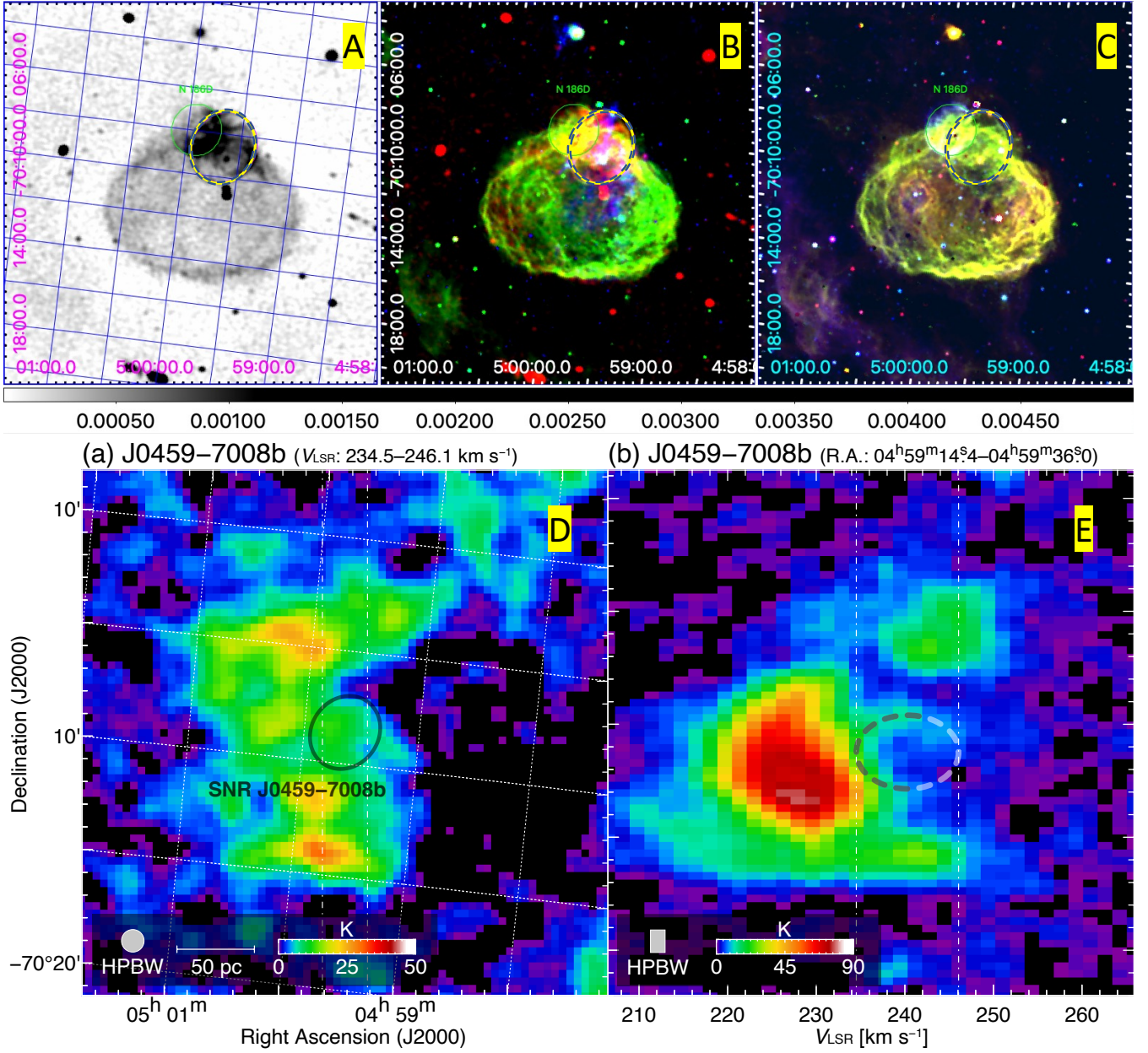


Figure A5. J0459-7008b: Same as Fig. A1. Gray scale at the bottom of panel A (ASKAP image) is from 0 to 5 mJy beam $^{-1}$.

ity to this source, with 10 located inside the measured extent. Our H α map and the $p - v$ diagram show a clear cavity in which this object may be expanding.

A8 MCSNR J0522-6543

This candidate has a shell morphology with ring brightened regions in the north-east and south-west (Figs. 4, A8 and A9). It also has a dominant bright central source. The intriguing central position of this point-like source suggests the possible presence of a PWN, but we can not exclude a random background galaxy. This region was catalogued by Davies et al. (1976) and given the reference DEM L155A. They described the source as a bright diffuse circular region 2.5×2.5 arcmin 2 , which is fractionally smaller than our diameter measurement of 2.85×2.63 arcmin 2 . The MCELS image

has an enhanced [SII]/H α ratio of just slightly above 0.4 in the source's north-east region. There are 15 OB star candidates located within, or in close proximity to this source with 7 inside the projected boundary and four of these just off centre. Also, some 18 arcsec from the centre is the well studied young star cluster KMHK 833 (Kontizas et al. 1990). MCSNR J0522-6543 shows clear evidence of expanding inside a cavity or bubble-like structure in the H α map and the $p - v$ diagram. These H α clouds are most likely associated with the SNR as they seem to be positioned along the edge of the somewhat larger expanding H α bubble (see Fig. A8 panels D and E).

We measured flux densities (see Table A1) and obtained a spectral index of $\alpha = -0.51 \pm 0.05$ for MCSNR J0522-6543 and for the central bright point source we estimate $\alpha = -1.04 \pm 0.04$. These results indicate the spectral index is typical of LMC SNRs (Bozzetto

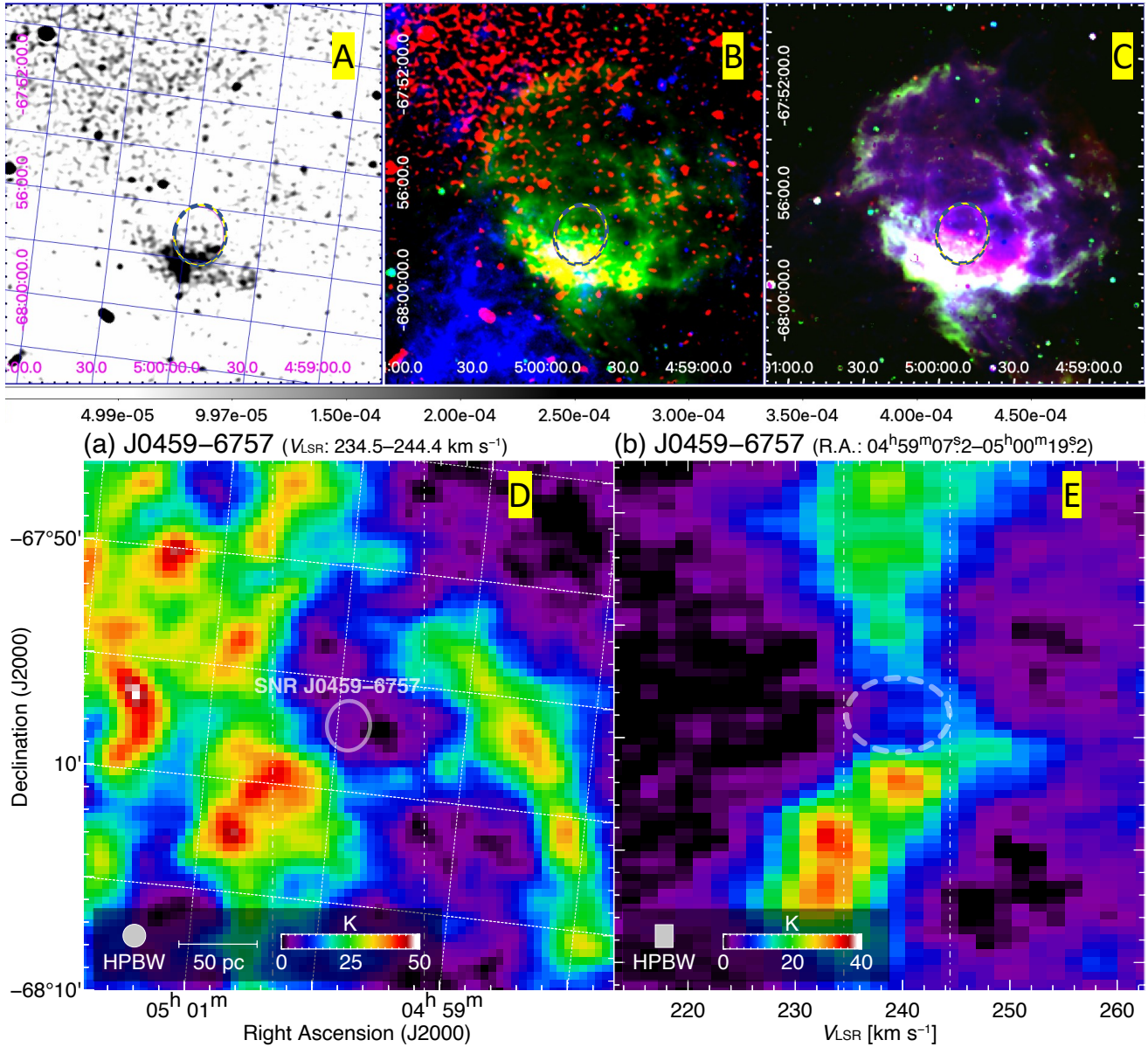


Figure A6. J0459–6757: Same as Fig. A1. Gray scale at the bottom of panel A (ASKAP image) is from 0 to 0.5 mJy beam⁻¹.

et al. 2017) while the central bright source is most likely an unrelated background object (active galactic nucleus (AGN) or radio quasar). However, as discussed above (Section 3), missing short spacing may influence our flux densities estimates. This is especially true at the higher frequencies (ATCA; 5500 and 9000 MHz; Fig. A9) where our flux density measurements could be underestimated. Filipović et al. (2022) suggest these could be as much as ~15–20 per cent (in flux density) which translates to a flattening of the spectral index by about 0.1 to $\alpha \sim -0.41$. Nonetheless, this would still allow the spectral index for MCSNR J0522–6543 to remain in a range acceptable for SNRs classification.

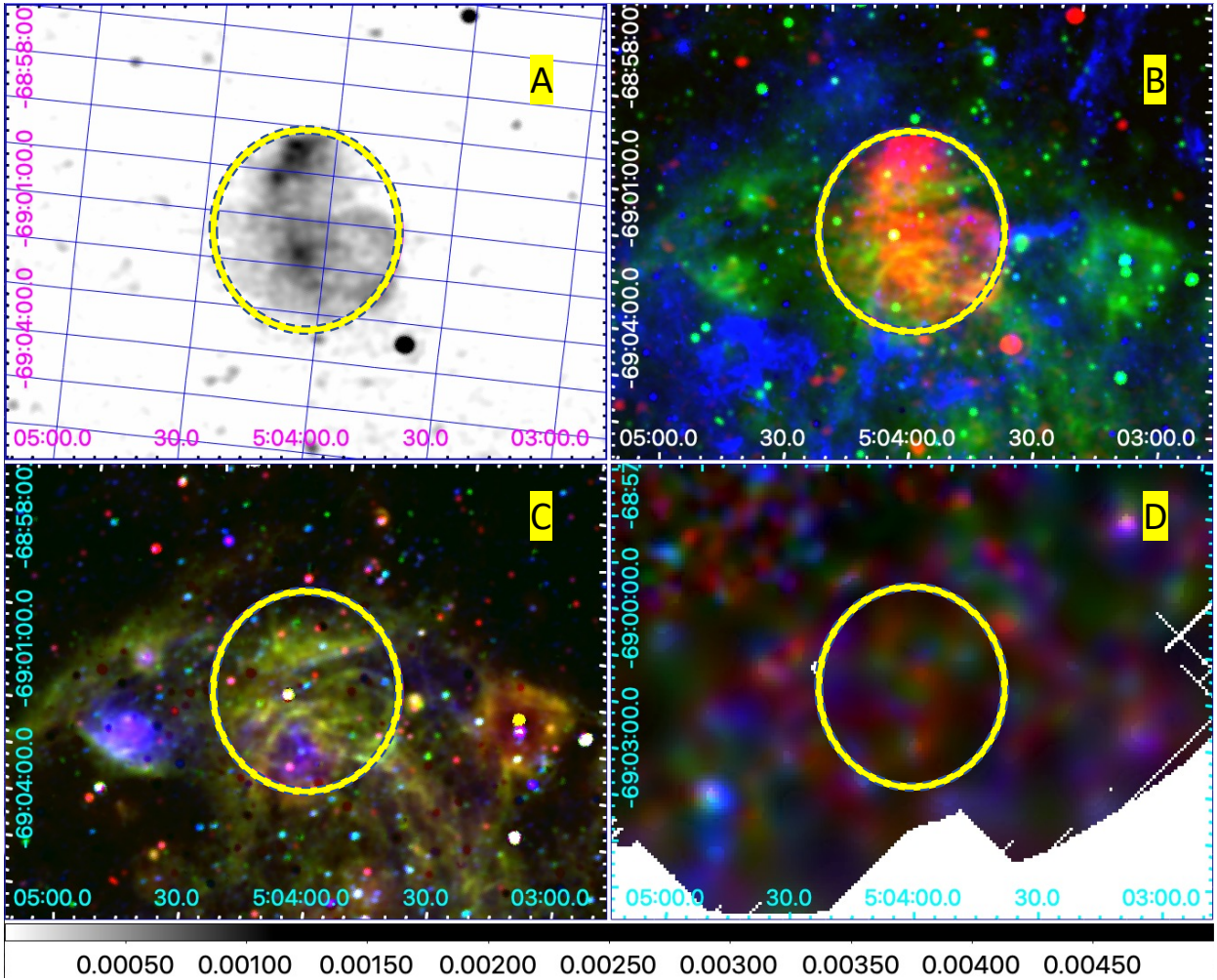
MCSNR J0522–6543 satisfies two out of three criteria (optical $[SiI]/H\alpha > 0.4$ and radio spectral index $\alpha < -0.5$) to be a bona fide SNR. Future deep X-ray observations of this region may reveal more about the true nature of this source.

Table A1. Radio flux density measurements for MCSNR J0522–6543 and for the central point source J052254.7–654311.

	MCSNR J0522–6543	J052254.7–654311
$S_{888\text{ MHz}}$ (mJy)	33.1 ± 0.7	3.52 ± 0.11
$S_{1384\text{ MHz}}$ (mJy)	31.3 ± 0.4	2.10 ± 0.05
$S_{2100\text{ MHz}}$ (mJy)	19.8 ± 0.4	1.47 ± 0.05
$S_{5500\text{ MHz}}$ (mJy)	15.1 ± 0.4	0.55 ± 0.05
$S_{9000\text{ MHz}}$ (mJy)	10.2 ± 0.4	0.29 ± 0.05
$\alpha \pm \Delta\alpha$	-0.51 ± 0.05	-1.04 ± 0.04

A9 J0534–6720

This is the second largest candidate proposed in this study at $D = 70$ pc and appears with a complex shell morphology that includes areas of enhanced emission around the rim (Figs. 4 and A10). The radio shell is most pronounced to the south. There is also noticeable



(a) J0504-6901 (V_{LSR} : 260.9–274.1 km s⁻¹)

(b) J0504-6901 (R.A.: 05^h03^m16^s8–05^h04^m31^s2)

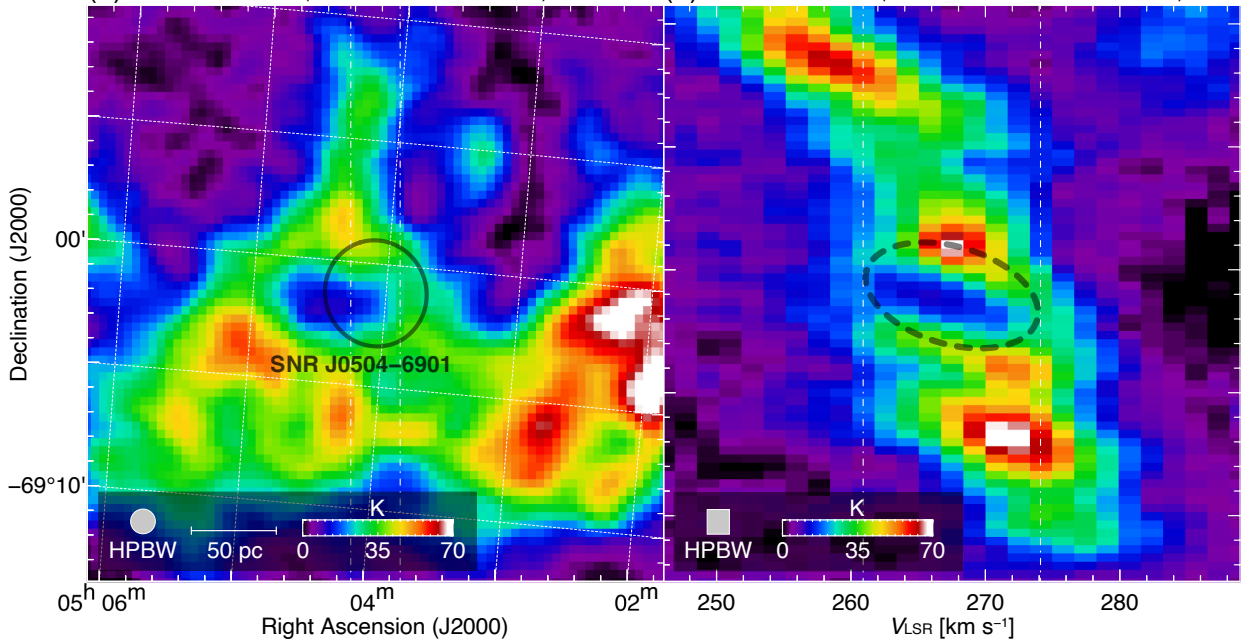


Figure A7. J0504-6901: Same as Fig. A2. We note an image artefact in the X-ray (D) panel. Gray scale at the bottom of panel A (ASKAP image) is from 0 to 5 mJy beam⁻¹.

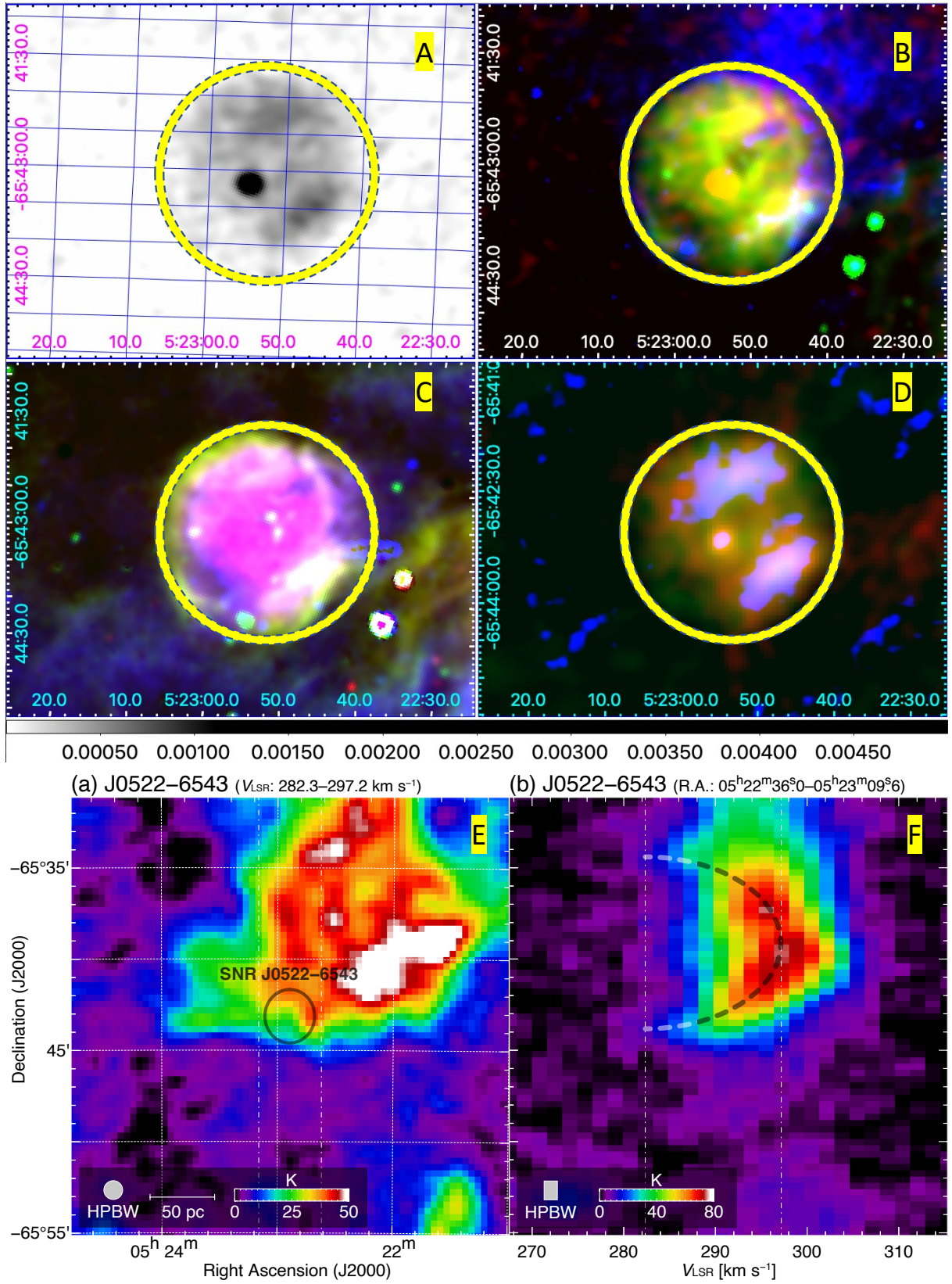


Figure A8. MCSNR J0522-6543: (Top) Left (A): New ASKAP 888 MHz radio image at 13.9×12.1 arcsec² resolution. Gray scale at the bottom of panel A (ASKAP image) is from 0 to 5 mJy beam⁻¹. Right (B): RGB image where ATCA 2100 MHz radio image is in red, H α (green) and Spitzer LMC-SAGE at 8 μ m in blue. (Middle) Left (C): MCELS optical RGB image where H α (red), [SII] (green), & [OIII] (blue). Right (D): RGB image made from our new ATCA observations at 2100 MHz (red), 5500 MHz (green) and 9000 MHz (blue). All images are smoothed to the resolution of 2100 MHz image (20.95×16.60 arcsec²). The blue-yellow ellipse indicates positions of here proposed SNR. (Bottom) Left (E): Integrated intensity map of HI obtained with ATCA & Parkes (Kim et al. 2003). Right (F): Position-velocity diagram of HI.

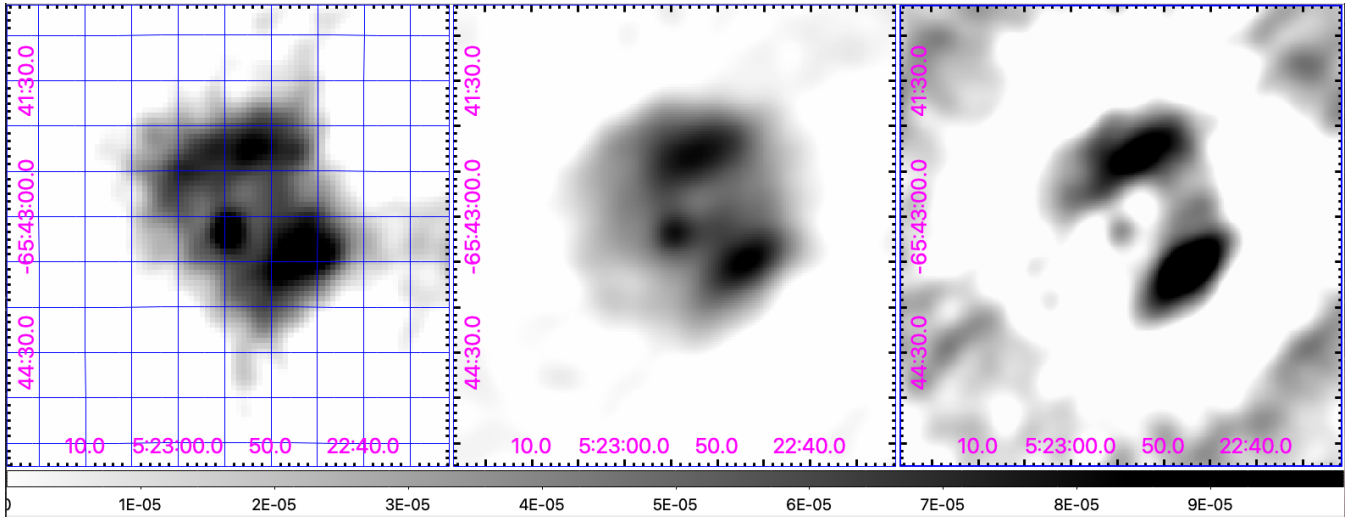


Figure A9. ATCA images of MCSR J0522–6543 at 2100 MHz (left), 5500 MHz (middle) and 9000 MHz (right). All images are smoothed to the resolution of 2100 MHz image (20.95×16.60 arcsec²). Gray scale at the bottom is from 0 to 0.1 mJy beam⁻¹.

radio emission towards the west and slightly beyond the presumed circular boundaries of this SNR candidate that might be an integral part of the object. Its pear-like appearance is reminiscent of the Galactic SNR Cygnus Loop, which might consist of two SNRs (Uyaniker et al. 2002). There are 45 OB star candidates located within 100 pc of the source, but only one appears within the bounds of the emission. While the enhanced radio-to-H α ratio shows a large ring-like shell, no real traces of radiative shocks are seen in any MCELS band. But, the H I map and the $p - v$ diagram show a clear cavity structure at this position which warrants an SNR candidate classification. This object is therefore potentially an excellent example of an SNR expanding inside the large scale cavity of a (super)bubble.

A10 J0534–6700

This faint and almost circular shell morphology source (Figs. 4 and A11) is located at the eastern end of the large LMC4 supergiant shell (Meaburn 1980). There are 325 OB star candidates located within, or in close proximity to, this source. As for the number of other sources in our sample, we can see a clear cavity in our H I and $p - v$ diagram. The absence of an optical detection is intriguing, but expected for this possible late evolutionary stage SNR.

A11 J0542–6852

The radio emission of this candidate appears with a faint and slightly elongated shell-like morphology (Figs. 4 and A12). The remnant also appears to show faint X-ray emission in the soft and medium bands of *XMM-Newton* survey images as well as some filaments associated with [O III] emission. There are 40 OB star candidates located within, or in close proximity to this source. J0542-6852 has possibly two counterparts of wind bubbles in the $p - v$ diagram, but these spatial extents in declination are slightly offset from the SNR position. It is, therefore, possible that these two expanding bubbles are not from the SNR candidate, but were caused by other events such as past activities of nearby OB associations.

A12 J0543–6928

This source exhibits a complex shell morphology elongated in the NW-SE direction (Figs. 4 and A13). It has a very strong enhancement in the radio-to-H α ratio image which suggests the structure is non-thermal. However, no counterpart is seen in the MCELS, nor in our deep *XMM-Newton* images. There are 34 OB star candidates located within, or in close proximity to, this source, though, only one of these lies in the bounds of the emission.

A13 J0543–6923

Emission from this source follows a ring morphology (Figs. 4 and A14). Brightening in our radio/H α /IR image (panel B of Fig. A14) can be seen in the north and east where the source appears to be colliding with emission from the H I cloud (panel E of Fig. A14). Indeed, our $p - v$ diagram shows a clear cavity where this SNR candidate may be expanding. There are 31 OB star candidates located within, or in close proximity to, this source. However, only one is within the bounds of the emission – located at an area of brightening in the north-east. We note a significant amount of possible non-thermal radio emission beyond the proposed boundaries (east) of this SNR candidate. While we cannot exclude the association of these regions with the proposed remnant J0543–6923, we suggest it could be part of a larger and non-related (super)bubble structure.

A14 J0543–6906

This source is the largest in our study ($D = 96$ pc) and exhibits a ring-like morphology with significant brightening on the western rim (Figs. 4 and A15). While there are a large number of optical filaments across this region, we cannot associate any of them with this potentially largest SNR candidate in our sample. Unfortunately, our *XMM-Newton* images of this region are not sensitive enough to clearly confirm its nature. There are 50 OB star candidates located within, or in close proximity to this source, with eight inside the measured extent of emission. J0543–6906 is likely located in the

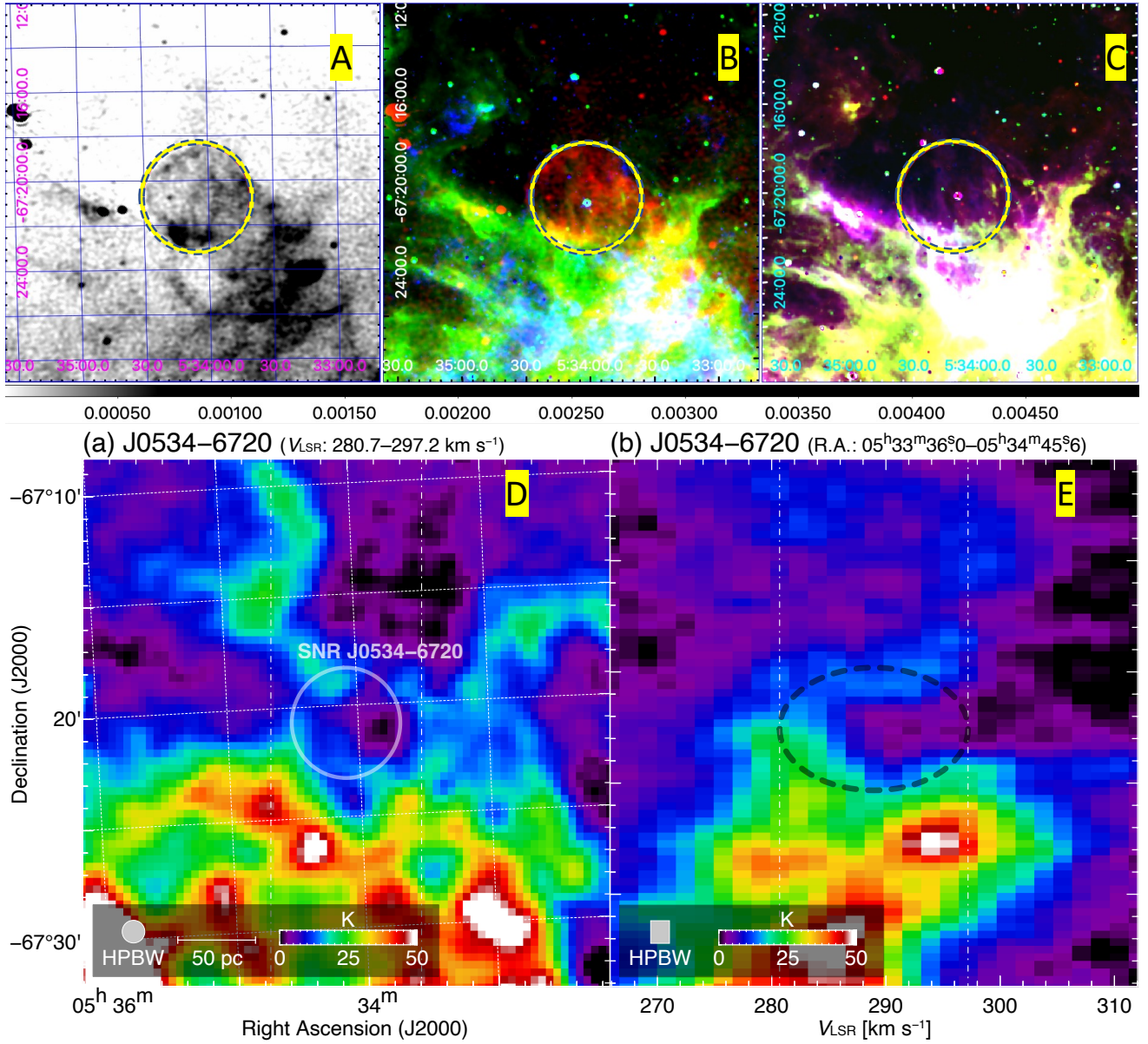


Figure A10. J0534-6720: Same as Fig. A1. Gray scale at the bottom of panel A is from 0 to 5 mJy beam⁻¹. The central star visible in optical images is a Galactic foreground star HD 269767 and is not related to the source.

large wind-(super)bubble that was formed by massive star cluster(s); its size is significantly larger than that of a single supernova.

This paper has been typeset from a TeX/LaTeX file prepared by the author.

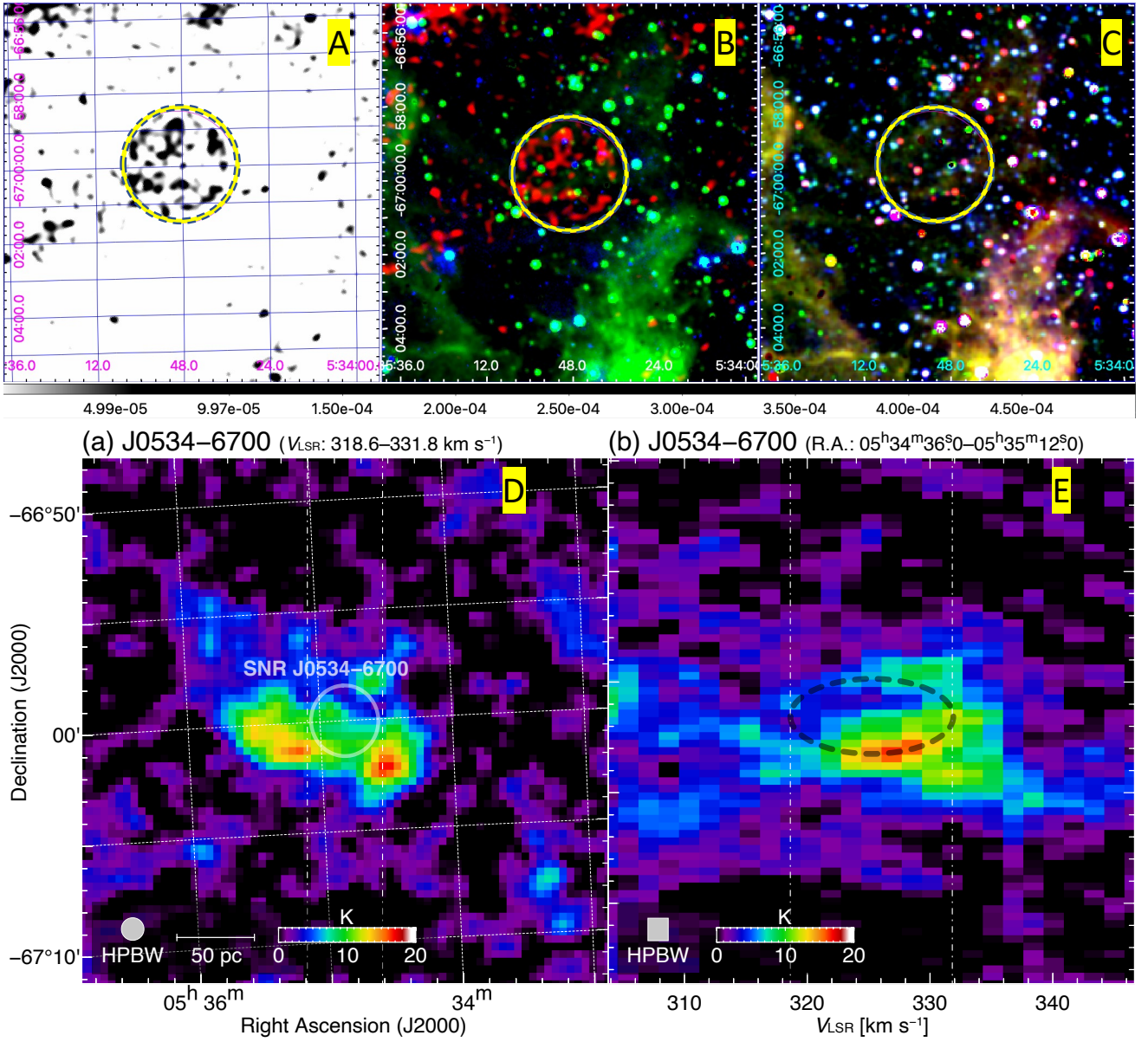


Figure A11. J0534-6700: Same as Fig. A1. Gray scale at the bottom of panel A (ASKAP image) is from 0 to $0.5 \text{ mJy beam}^{-1}$.

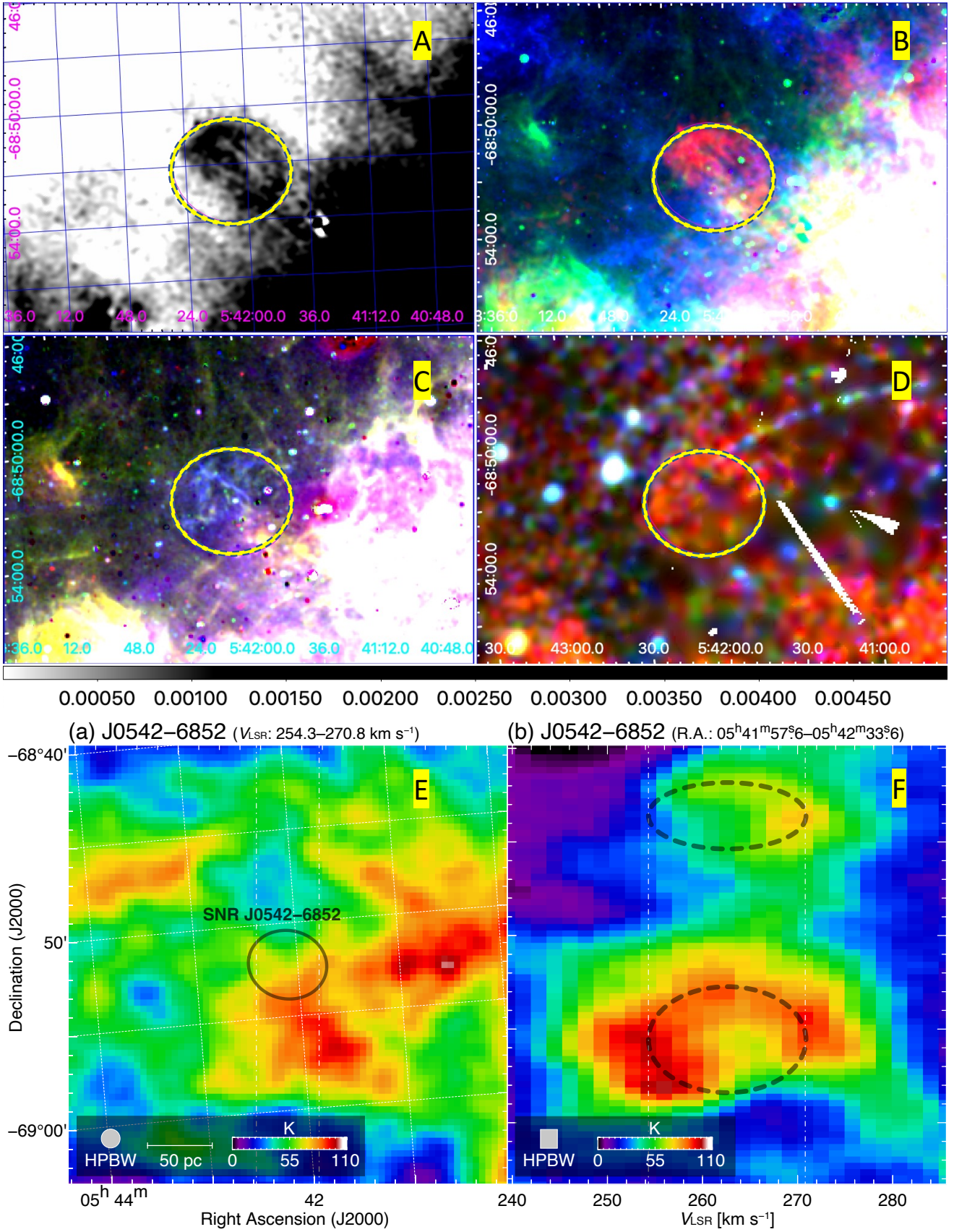
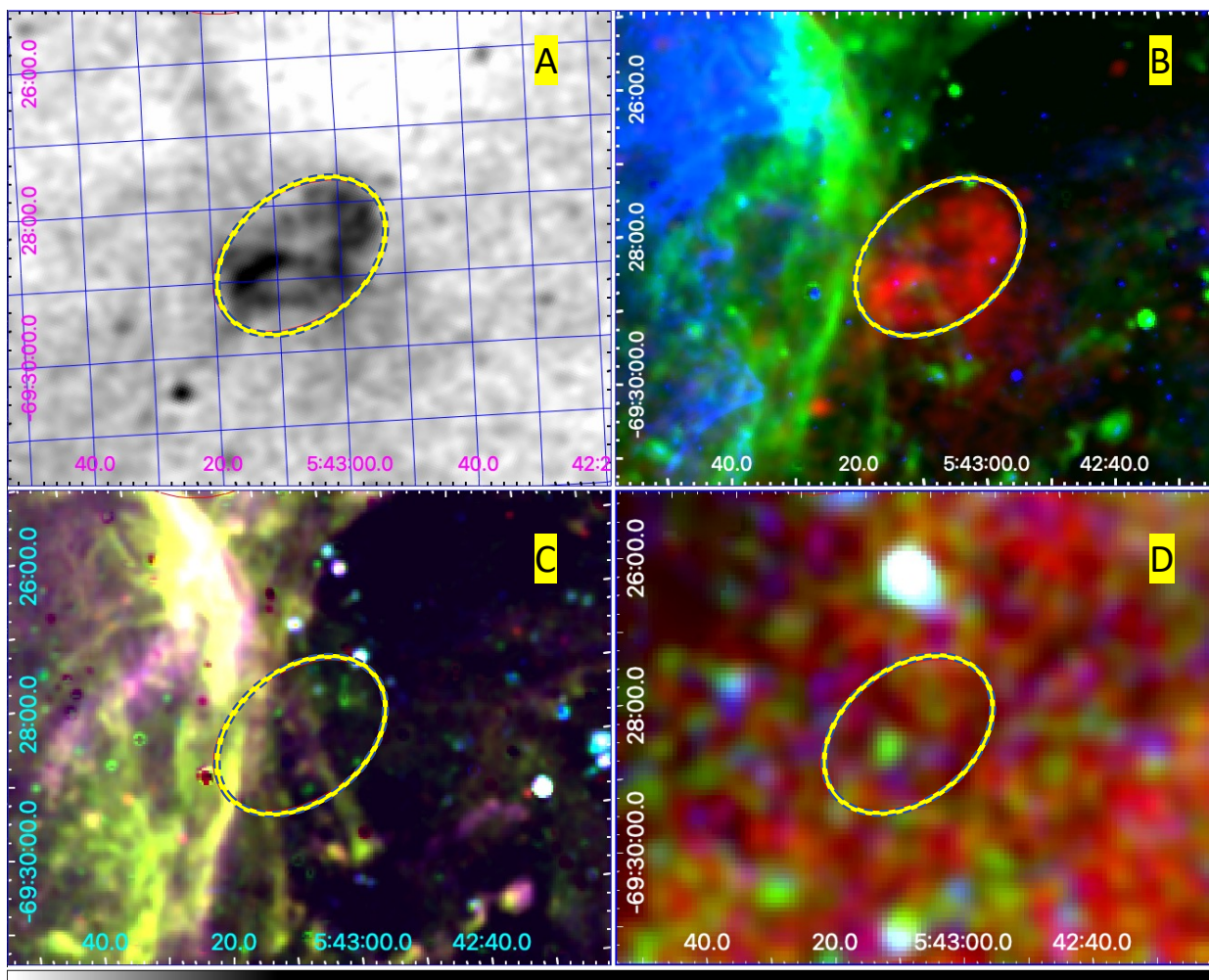


Figure A12. J0542-6852: Same as Fig. A2. Gray scale at the bottom of panel A (ASKAP image) is from 0 to 5 mJy beam⁻¹. We note an image artefact in the X-ray (D) panel.



0.00050 0.00100 0.00150 0.00200 0.00250 0.00300 0.00350 0.00400 0.00450
 (a) J0543-6928 (V_{LSR} : 254.3-267.5 km s $^{-1}$) (b) J0543-6928 (R.A.: 05 $^{\text{h}}$ 42 $^{\text{m}}$ 50 $^{\text{s}}$.4-05 $^{\text{h}}$ 43 $^{\text{m}}$ 43 $^{\text{s}}$.2)

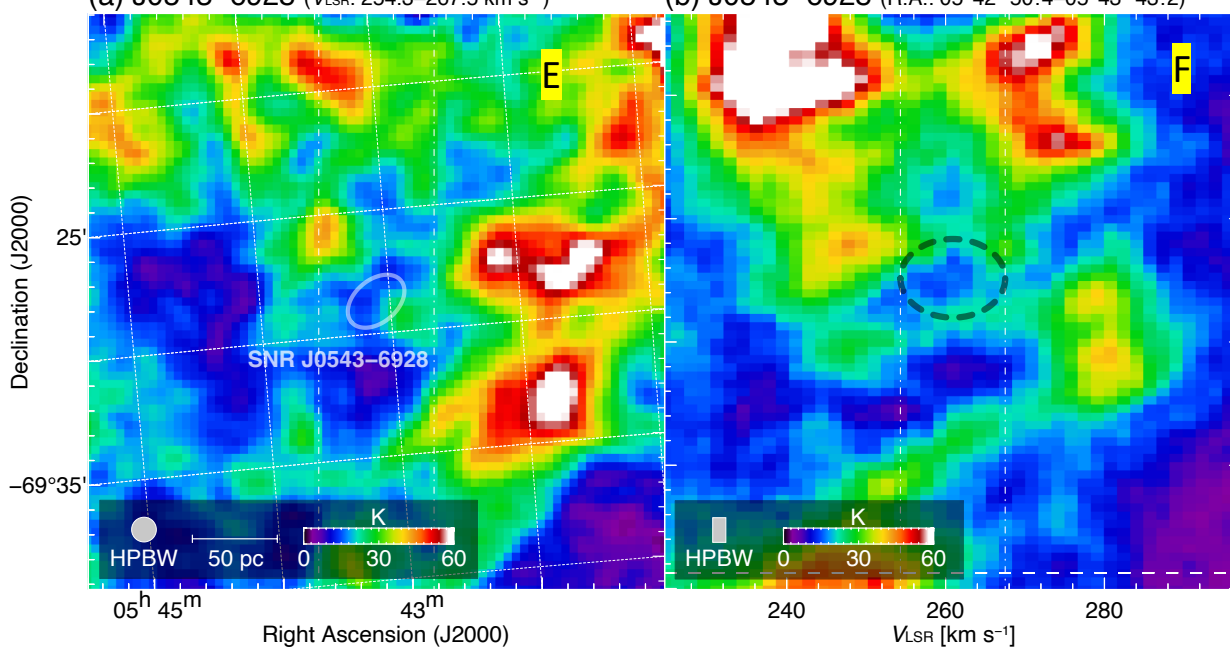
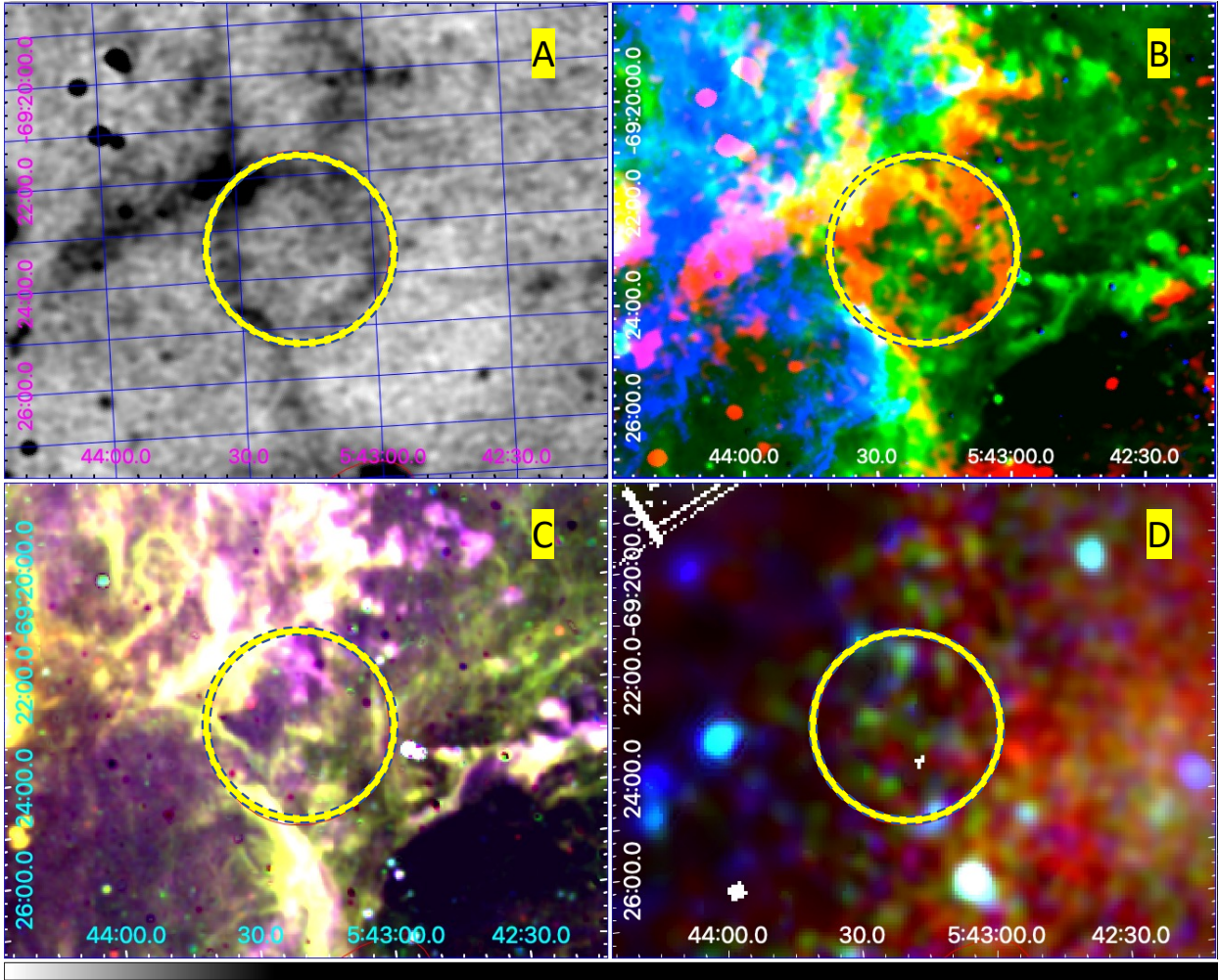


Figure A13. J0543-6928: Same as Fig. A2. Gray scale at the bottom of panel A (ASKAP image) is from 0 to 5 mJy beam $^{-1}$.



0.00050 0.00100 0.00150 0.00200 0.00250 0.00300 0.00350 0.00400 0.00450
 (a) J0543-6923 (V_{LSR} : 242.8–274.1 km s $^{-1}$) (b) J0543-6923 (R.A.: 05 $^{\text{h}}$ 43 $^{\text{m}}$ 00 $^{\text{s}}$ 0–05 $^{\text{h}}$ 43 $^{\text{m}}$ 52 $^{\text{s}}$ 8)

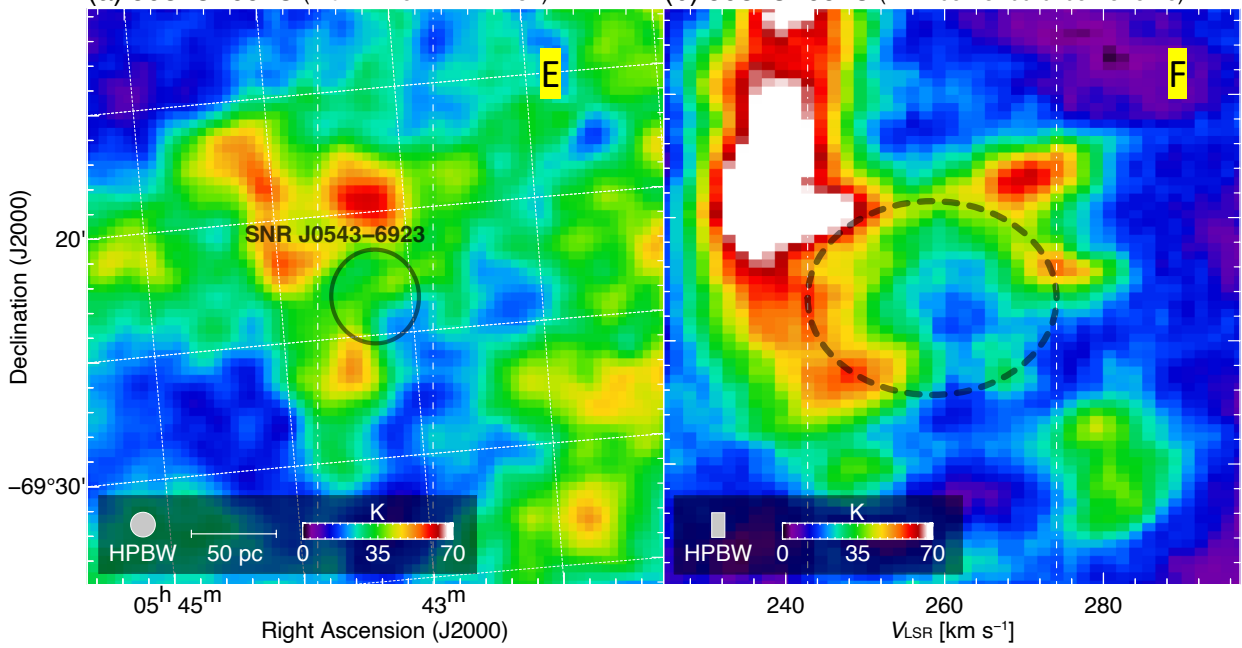


Figure A14. J0543-6923: Same as Fig. A2. Gray scale at the bottom of panel A (ASKAP image) is from 0 to 5 mJy beam $^{-1}$. We note an image artefact in the X-ray (D) panel.

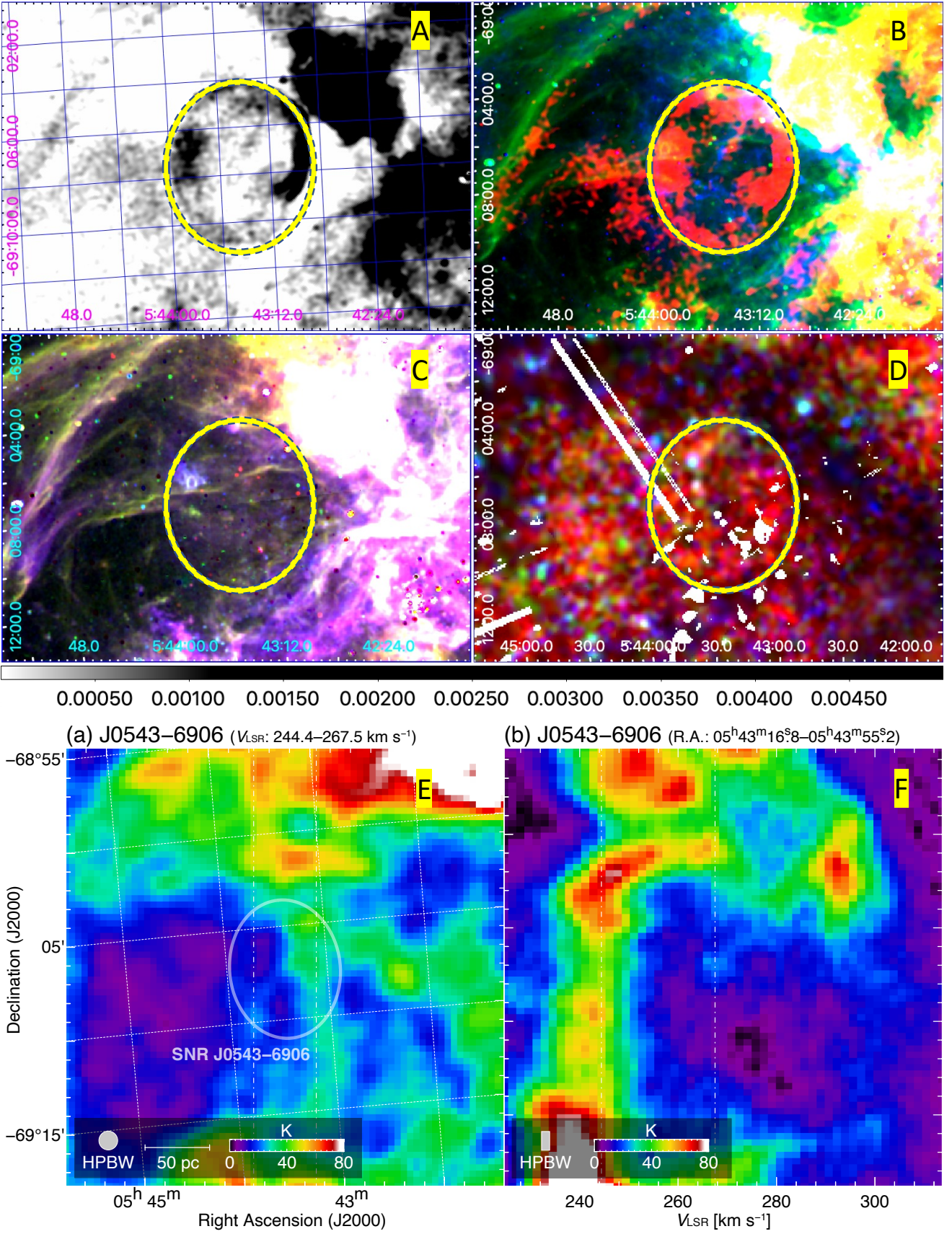


Figure A15. J0543-6906: Same as Fig. A2. Gray scale at the bottom of panel A (ASKAP image) is from 0 to 5 mJy beam⁻¹. We note image artefacts in the optical (C) and X-ray (D) panels.